Engineered Metal Oxide Nanostructures for Highly Sensitive and Selective Toxic Gas Sensing

MS (Research) Thesis

By

SOURAJIT MUKHERJEE



DISCIPLINE OF ELECTRICAL ENGINEERING

INDIAN INSTITUTE OF TECHNOLOGY INDORE

APRIL 2026

Engineered Metal Oxide Nanostructures for Highly Sensitive and Selective Toxic Gas Sensing

A THESIS

Submitted in fulfillment of the
requirements for the award of the degree
of

Master of Science (Research)

by

SOURAJIT MUKHERJEE



DISCIPLINE OF ELECTRICAL ENGINEERING
INDIAN INSTITUTE OF TECHNOLOGY INDORE
APRIL 2026

INDIAN INSTITUTE OF TECHNOLOGY INDORE

CANDIDATE'S DECLARATION

I hereby certify that the work which is being presented in the thesis entitled **Engineered Metal Oxide Nanostructures for Highly Sensitive and Selective Toxic Gas Sensing** in the fulfillment of the requirements for the award of the degree of **MASTER OF SCIENCE (RESEARCH)** and submitted in the **DISCIPLINE OF ELECTRICAL ENGINEERING, Indian Institute of Technology Indore**, is an authentic record of my own work carried out during the time period from July 2024 to March 2026 under the supervision of **Prof. Shaibal Mukherjee**, Professor, Electrical Engineering, IIT Indore

The matter presented in this thesis has not been submitted by me for the award of any other degree of this or any other institute.

Sourajit Mukherjee 25/5/26
Signature of the student with date
SOURAJIT MUKHERJEE

This is to certify that the above statement made by the candidate is correct to the best of my/our knowledge.

S. Mukherjee
Signature of the Supervisor of
MS (Research) thesis with date
(Prof. Shaibal Mukherjee)

Sourajit Mukherjee has successfully given his/her MS (Research) Oral Examination held on _____.

28/5/2026
Signature of Chairperson (OEB) with date

S. Mukherjee
Signature(s) of Thesis Supervisor(s) with date

Saptarshi Ghosh 25-05-2026
Signature of Convener, DPGC with date

25/5/26
Signature of Head of Discipline with date

ACKNOWLEDGEMENTS

I would like to thank my esteemed supervisor **Prof. Shaibal Mukherjee**, Professor, Department of Electrical Engineering IIT Indore for his invaluable supervision, support and tutelage during the course of MS(Research) degree. His profound knowledge, insightful suggestions, and meticulous supervision have been instrumental in shaping this work. I am deeply thankful for his patience, motivation, and continuous mentorship, which not only helped me in completing this research but also contributed significantly to my academic and personal development.

I sincerely thank **Prof. Suhas S. Joshi**, Director of IIT Indore, for enabling access to the necessary experimental facilities. I also acknowledge with appreciation the assistance provided by the Sophisticated Instrumentation Center (SIC) at IIT Indore for carrying out the XRD, SEM, and EDX analyses.

I would like to express my sincere gratitude to **Prof. Sharath Sriram** of the Functional Materials and Microsystems Research Group, RMIT University, Australia, for generously providing access to lithography facilities essential for this work.

I am extremely grateful to my family members, **Mr. Jaideep Mukherjee** (Father) and **Mrs. Sumana Mukherjee** (Mother), for their unconditional love, constant support, and encouragement throughout my life. Their unwavering belief in me and their presence through every phase of my journey have been a source of strength, enabling me to overcome challenges and pursue my goals with confidence. I would like to express my heartfelt gratitude to **Ms. Jyotsna Mukherjee** (paternal grandmother) and **Ms. Bani Chattaraj** (maternal grandmother) for their constant blessings, love, and best wishes. Their unwavering support and encouragement have been a guiding force in my life, and their blessings have played a crucial role in all that I have achieved today.

I would like to express my sincere gratitude to **Dr. Chandrabhan Patel** for his invaluable support in my research work and for helping me develop a strong foundation in critical thinking, which has greatly contributed to my academic growth. I am deeply thankful to **Ms. Poonam Bajoria** for her constant encouragement, insightful discussions, and unwavering support during challenging times. Being by my side like an elder sister, she has been a pillar of strength, motivating me through repeated setbacks and uplifting my spirits, which has been truly instrumental in keeping me focused and inspired throughout this journey. I would also like to extend my heartfelt thanks to **Mr. Vikash Kumar Verma, Mr. Brahmadutta Mahapatra, Mr. Animesh Paul**, and **Mr. Shorinjiryu Bhowmick** for their continuous support, guidance, and willingness to help in every challenging situation. Their contributions have played a significant role in helping me understand various aspects of research, starting from the fundamentals. I am equally grateful to other lab members-**Dr. Sumit Chaudhary, Dr. Mayank Dubey, Dr. Shivendu Mishra, Mr. Saurabh Yadav, Mr. Lokesh Kumar Hindoliya, Mr. Ajit Yadav, Ms. Usha Phogat, Mr. Mohit Kumar, and Mr. Pranav Mahajan**-for their support, cooperation, and for creating a collaborative and encouraging research environment.

This Thesis is Dedicated

To

GOD, My Family and My Loved Ones

ABSTRACT

This thesis presents a comprehensive study on the effects of surfactant-assisted synthesis and doping on transition metal oxides (TMOs), and their influence on toxic gas sensing performance, aimed at the development of highly selective and sensitive gas sensors. The optimization and characterization of the fabricated TMOs are specifically focused on enhancing sensing performance in terms of sensitivity, selectivity, response and recovery times, and long-term stability. Among various metal oxide sensing materials, cobalt oxide (Co_3O_4) has emerged as a promising candidate due to its excellent catalytic activity, chemical stability, and favourable electronic properties. Co_3O_4 is a p-type semiconductor that exhibits notable gas sensing behaviour toward different target gases. In this thesis, CTAB-assisted molybdenum (Mo)-doped Co_3O_4 nanostructures have been synthesized using a hydrothermal method and investigated as a sensing material for the detection of carbon monoxide (CO) gas. Carbon monoxide is a highly toxic and colourless gas that poses serious health hazards even at low concentrations, making its accurate detection extremely important.

To optimize and further improve the sensing performance, different concentrations of Mo dopant were incorporated into the Co_3O_4 structure, and a surfactant (CTAB) was introduced during the synthesis process to assist in controlling the nanostructure morphology. The sensing characteristics were systematically investigated, and the results indicate that the sensor performance strongly depends on the synergistic effect of Mo doping and CTAB-assisted nanostructure formation. Among the synthesized samples, the CTAB-assisted 2.5 mol% Mo-doped Co_3O_4 sensor exhibited the best sensing performance toward CO gas, showing an exceptionally high response of 4188% at a CO concentration of 100 ppm. Furthermore, the fabricated sensor demonstrated a remarkably low limit of detection of 4 ppb, indicating its capability to detect trace levels of CO gas. The sensor also exhibited excellent repeatability and long-term stability. In addition, the sensing performance remained reliable under humid environmental conditions and the sensor displayed relatively short response and recovery times.

To further evaluate the performance of the developed sensor, a comparative study was carried out with a commercially available CO sensor (MQ7). The commercial sensor was carefully disassembled and its internal components were systematically examined to understand its structure and operating mechanism. Sensitivity and selectivity analyses were then performed and compared with the fabricated sensor. The results revealed that the developed CTAB-assisted Mo-doped Co_3O_4 sensor exhibits significantly superior sensitivity and selectivity compared to the commercial MQ7 sensor.

Overall, the results presented in this thesis demonstrate that CTAB-assisted Mo-doped Co_3O_4 nanostructures are highly promising sensing materials for the detection of CO gas. The enhanced

sensing performance, combined with excellent stability and improved selectivity, highlights the potential of this material for the development of next-generation gas sensing devices for environmental monitoring and industrial safety applications.

LIST OF PUBLICATIONS

- Outcomes from MS (Research) thesis work:

1. **S. Mukherjee**, V.K. Verma, C. Patel, S. Chaudhury, P. Bajoria, S. Bhowmick, R.T. Ako, S. Sriram, and S. Mukherjee, "Room-Temperature CO Detection Using Facile CTAB-Assisted Mo Doped Co_3O_4 Nanoflowers," Sensors and Actuators B: Chemical (Accepted)

- Other outcomes outside of the MS (Research) thesis work:

1. V.K. Verma, C. Patel, **S. Mukherjee**, S. Bhowmick, S.N. Upadhyay, V. Kumar, R.T. Ako, S. Sriram, S. Pakhira, and S. Mukherjee, "Ultra-Sensitive and Selective Room Temperature H_2S Detection Using Pd-Doped MoS_2 Via APCVD," Sensors and Actuators B: Chemical (Accepted).

2. V.K. Verma, **S. Mukherjee**, Usha, S. Bhowmick, B. Mahapatra, P. Bajoria and S. Mukherjee, "Controlled Shape Evolution and Layer Engineering of WS_2 via Optimized Multi Zone APCVD Growth," npj 2D Materials (Under Review)

3. P. Bajoria, S. Bhowmick, **S. Mukherjee,** S. Chaudhury, V.K. Verma, R.T. Ako, S. Sriram, and S. Mukherjee, "Non-Enzymatic Chemiresistive Detection of Trace-Level Creatinine Using Tailored CuO Nanoflakes for Kidney Health Monitoring," Microchemical Journal (Under Review).

Table of Contents

ABSTRACT **1**

LIST OF PUBLICATIONS ..... **iii**

LIST OF FIGURES ..... **vi**

LIST OF TABLES ..... **viii**

LIST OF ABBREVIATIONS ..... **ix**

Chapter 1: Introduction and Fundamental Concepts **1**

1.1 Introduction of Gas Sensors 1

1.2 Motivation 2

1.3. Types of Gas Sensors 3

1.3.1. Resistive Gas Sensor 3

1.3.2. Capacitive Gas Sensor 4

1.3.3. Optical Gas Sensor 6

1.3.4 Colorimetric Gas Sensor 6

1.3.5. Potentiometric Gas Sensor 7

1.3.6. Field-Effect Transistor (FET) Gas Sensor 8

1.4. Gas Sensing Terminology 9

1.5. Semiconducting Metal Oxide (MOX) Gas Sensors 11

1.5.1. General Sensing Mechanism 11

1.5.2. Factors Affecting Sensing Performance 14

1.6. Material Selection 21

1.6.1. Ideal Characteristics of a Gas Sensing Material 21

1.6.2. Why Metal Oxide? and Why Cobalt Oxide (Co_3O_4)? 22

1.7. Main Aim and Objectives 25

1.8. Thesis Organization 26

1.9. References 27

Chapter 2: Material Synthesis and Characterization for Gas Sensor Development **32**

2.1 Introduction 32

2.2 Synthesis Tools 33

2.2.1. Hydrothermal Synthesis 33

2.2.1.2. Instrumentation 35

2.3. Sensing Layer Characterization Techniques 38
2.3.1. X-Ray Diffraction Instrument 38
2.3.3. Raman Spectroscopy Instrument 44
2.3.4. X-Ray Photoelectron Spectroscopy (XPS) 46
2.3.5. Brunauer-Emmett-Teller (BET) Method 47
2.3.6. UV-Visible Spectroscopy 49
2.4. Dynamic Gas Sensing Setup 52
2.5. References 54
Chapter 3: Room-Temperature CO Detection Using CTAB-Assisted Mo-Doped Co_3O_4 Nanoflowers 57
3.1. Introduction 57
3.2. Experimental 59
3.2.1. Materials 59
3.2.2. Synthesis Process 59
3.2.3. Characterization 60
3.2.4. Device fabrication and gas sensing measurements 61
3.3. Results and Discussion 62
3.3.1. Surface Morphological Analysis 62
3.3.2. Sensing Performance Analysis 68
3.3.3. Sensing Mechanism 74
3.4. Conclusion 76
3.5. Reference 76
Chapter 4: Benchmarking Commercial Gas Sensors Against Lab-Developed Devices 85
4.1 Introduction 85
4.2. Structure and Working Principle of the MQ7 Commercial Gas Sensor 86
4.3. Disassembling, Electrical Characterization, and Comparative Analysis of the MQ7 Sensor 87
4.4. Conclusion 89
4.5. References 90
Chapter 5: Conclusion and Future Scope 92
5.1 Conclusion 92
5.2 Future Scope 93

LIST OF FIGURES

Fig. 1.1. Schematic of interdigitated electrode device used for chemiresistive based gas sensing 4
Fig. 1.2. Schematic illustration of capacitance-based gas sensor 5
Fig. 1.3: Schematic illustration of Optical Gase Sensor 6
Fig. 1.4. Schematic illustration of colorimetric based gas sensor 7
Fig. 1.5. Schematic of potentiometric gas sensor 8
Fig. 1.6. Schematic illustration of FET based gas sensor 9
Fig. 1.7. Adsorbed oxygen species on the sensor surface at different temperatures analyzed using FTIR, TPD, and EPR techniques. 12
Fig. 1.8. Schematic illustration of the energy band diagram and depletion layer variation in an n-type metal oxide (MOX) with adsorbed oxygen species under different environments: (a) vacuum, (b) air, (c) reducing gas atmosphere, and (d) oxidizing gas atmosphere 13
Fig. 1.9. Schematic illustration of the grain contact model and corresponding electronic band structure for (a) grain boundary contact and (b) neck contact. 15
Fig. 1.10. Schematic illustration models for grain size effect 16
Fig. 1.11. Schematic illustration of noble metal sensitization mechanisms in MOX sensors: (a) chemical sensitization and (b) electronic sensitization. 18
Fig. 1.12. Schematic diagram of Interdigitated Electrode Device 20
Fig. 2.1. Teflon-lined stainless-steel autoclave used in this thesis work. 36
Fig. 2.2. Flowchart of hydrothermal synthesis 38
Fig. 2.3. Photographic image of the Rigaku SmartLab Automated Multipurpose X-ray Diffractometer. 40
Fig, 2.4. Schematic illustration of the interaction between the incident electron beam and the sample surface. 41
Fig. 2.5. Schematic illustration of the FESEM–EDX working principle 43
Fig. 2.6. Photograph of the GEMINI SEM 360 scanning electron microscope used for surface morphology analysis. 44
Fig. 2.7. Photograph of the LabRAM Raman spectroscopy system used for Raman characterization. 45
Fig. 2.8. Photograph of the Thermo Scientific K-Alpha X-ray Photoelectron Spectrometer. 47
Fig. 2.9. Camera image of BET Surface Area Analyzer 48
Fig. 2.10. Digital image of UV-Vis Spectrometer 52
Fig. 2.11. Camera image of gas sensing setup. 54
Fig. 3.1. Schematic diagram for synthesis of CTAB assisted Mo doped Co_3O_4 60
Fig. 3.2. Camera image of IDEs. 62
Fig. 3.3. Schematic diagram of gas sensing setup used in this work 62
Fig. 3.4. FESEM images of (a) Pristine-Co_3O_4, (b) C-Co_3O_4, (c) C-Mo- Co_3O_4, (d) Magnified image of C-Mo-Co_3O_4 63
Fig. 3.5. (a) XRD spectrum of pristine-Co_3O_4 (I), C-Co_3O_4 (II), C-1.5% Mo- Co_3O_4 (III), C-2.5% Mo-Co_3O_4 (IV), C-3.5% Mo-Co_3O_4 (V); Nitrogen adsorption-desorption profile for (b) pristine- Co_3O_4, (c) C Co_3O_4, (d) C-2.5% Mo-Co_3O_4 64
Fig. 3.6. (a) XPS survey spectra of pristine Co_3O_4, (b) XPS survey spectra of CTAB assisted Mo doped Co_3O_4, (c) Co 2p, (d) Mo 3d, (e) O 1s spectra for pristine Co_3O_4, (f) O 1s spectra for CTAB assisted Mo-doped Co_3O_4 66

Fig. 3.7. Bandgap energy of (a) pristine-Co_3O_4, (b) C-Co_3O_4, (c) C 2.5%- Mo-Co_3O_4 and (d) Tabular representation of bandgap energy of pristine -Co_3O_4, C-Co_3O_4, C-2.5%-Mo-Co_3O_4. 67
Fig. 3.8: (a) Sensing performance of pristine-Co_3O_4 (I), C-Co_3O_4 (II), C- 1.5% Mo-Co_3O_4 (III), C-2.5% Mo-Co_3O_4 (IV), C-3.5% Mo-Co_3O_4 (V); (b) Selectivity analysis of C-2.5% Mo-Co_3O_4, (c) Response of C 2.5% Mo-Co_3O_4 at varying CO concentrations (d) Transient analysis of C-2.5% Mo-Co_3O_4. 69
Fig. 3.9: Operational analysis of C-2.5% Mo-Co_3O_4 (a) Relative humidity (RH) analysis (b) LoD and LoQ (c) Repeatability analysis for 10 cycles (d) Reproducibility with error bars. 70
Fig. 3.10. (a) Long term stability analysis of C-2.5% Mo-Co_3O_4, (b) I-V characteristics of pristine-Co_3O_4 (I), C-Co_3O_4 (II), C- 1.5% Mo-Co_3O_4 (III), C-2.5% Mo-Co_3O_4 (IV), C-3.5% Mo-Co_3O_4 (V); (c) I-V plot of C-2.5%-Mo-Co_3O_4 with and without exposure to CO and (d) Change in response with bias voltage for C-2.5%-Mo- Co_3O_4 72
Fig. 3.11. Schematic diagram of sensing mechanism 75
Fig. 4.1. (a) Image showing configuration of MQ7 sensor pins and structure of MQ7 sensor, (b) Image showing Internal structure of sensor under backlight illumination, (c) Internal structure of sensor (d) Internal and external structure of sensor in disassembled condition, (e) Heating coil and sensing material of the sensor 88
Fig. 4.2. Selectivity analysis of (a) 1st MQ7 sensor (b) 2nd MQ7 sensor (c) CTAB-assisted 2.5 mol% Mo-doped Co_3O_4 89

LIST OF TABLES

Table 1.1. Pristine and functionalized, doped Co_3O_4 gas sensor 25
Table 3.1: Comparative analysis with published literature 74

LIST OF ABBREVIATIONS

MOX	Metal Oxide Semiconductor
GC	Gas Chromatography
NDIR	Non-Dispersive Infrared
FID	Flame Ionization Detectors
CO	Carbon Monoxide
TMD	Transition metal dichalcogenides
MoS_2	Molybdenum Di Sulphide
WS_2	Tungsten Di Sulphide
$MoSe_2$	Molybdenum Di Selenide
WSe_2	Tungsten Di Selenide
MOSFET	Metal-Oxide-Semiconductor Field-Effect Transistor
FESEM	Field Emission Scanning Electron Microscopy
XRD	X-ray Diffraction
EDX	Energy Dispersive X-ray Spectroscopy
XPS	X-ray Photoelectron Spectroscopy
BET	Brunauer-Emmett-Teller
UV	Ultraviolet
CTAB	Cetyl Trimethyl Ammonium Bromide
CCD	Charge Coupled Devices
PPM	Parts Per Million
PPB	Parts Per Billion
PID	Proportional-Integral-Derivative
MFC	Mass Flow Controller
SO_2	Sulphur Di Oxide
NO_2	Nitrogen Di Oxide
NH_3	Ammonia
NO	Nitric Oxide
CO_2	Carbon Di Oxide
RH	Relative Humidity
Co_3O_4	Cobalt Oxide
RT	Room Temperature
LOD	Limit of Detection
LOQ	Limit of Quantification

Chapter 1
Introduction and Fundamental Concepts
1.1 Introduction of Gas Sensors

The rapid growth in population, expansion of industrial activities, and continuous technological advancements are significantly transforming modern lifestyles and increasing the demand for improved environmental monitoring and safety solutions. The escalating levels of air pollution are contributing to serious health risks and causing significant environmental degradation, thereby posing a major challenge to public health and ecological sustainability. In this context, gas sensors offer an effective solution by enabling the rapid identification and continuous assessment of toxic gases across various environments, thereby supporting pollution control, industrial safety, and public health protection. Conventional gas analyzers such as gas chromatography (GC), non-dispersive infrared (NDIR) analyzers, flame ionization detectors (FID), chemiluminescence analyzers, paramagnetic oxygen analyzers, and early electrochemical systems were bulky, expensive, power-intensive, and unsuitable for real-time portable monitoring, thereby necessitating the development of compact and cost-effective gas sensors. These gas sensors can be deployed across a wide range of settings, including urban and rural environments for air quality assessment, industrial facilities for leakage detection and process safety, residential and commercial buildings for indoor air quality assessment, healthcare and laboratory environments for safety assurance, and transportation systems for emission control, thereby supporting regulatory compliance, pollution mitigation, and the protection of human health and infrastructure. With the continuous introduction of advanced technologies and the expansion of smart infrastructure, the demand for such gas sensors is steadily increasing to enable real-time monitoring, enhanced safety, and intelligent environmental management. This thesis focuses on the development of nanostructure-based high-performance gas and VOC sensors, with particular emphasis on the detection of carbon monoxide (CO) and methanol vapors, respectively.

1.2 Motivation

Historically, efforts to detect toxic and combustible gases in coal mines were driven by the need to protect workers, as these gases are flammable, toxic, and can also reduce oxygen levels. One of the earliest methods involved the use of open flame safety lamps to indicate the presence of combustible gases. In a gas-rich atmosphere, the flame would burn more brightly or elongate, whereas reduced oxygen levels would cause the flame to dim or extinguish. However, this method posed significant safety risks, as the presence of excessive combustible gases could ignite and lead to catastrophic explosions, making it an inherently unsafe detection technique. Another early safety measure involved the use of small caged birds to detect hazardous atmospheric conditions in mines. This practice relied on the premise that toxic gases would affect the birds more rapidly than humans, thereby serving as an early warning indicator for miners. However, this method lacked reliability and precision, as the birds were not sensitive to all types of toxic gases present in the environment and provided no quantitative information about gas concentrations. A significant advancement in gas sensor technology occurred in the 1920s. In 1927, Dr. Oliver Johnson developed the first commercial gas sensor and introduced a method for detecting flammable gases using a platinum catalyst [1]. In 1960, a surge in demand for improved gas sensors was observed in Japan, primarily due to disasters involving explosions of liquefied petroleum (LP) gas cylinders. In 1962, Seiyama et al. introduced a novel gas sensor based on semiconducting metal oxides, employing zinc oxide as the sensing material [2]. The operating principle of this sensor relied on semiconductor catalysis, in which the adsorption of a target gas caused a change in the electrical resistance of the zinc oxide film. This discovery stimulated extensive research and development in gas sensors based on metal oxide semiconductor by various research groups. Following this, Taguchi developed a gas sensor utilizing metal-doped tin oxide and successfully brought it to commercial use in 1969. These developments

contributed to a decline in gas-related accidents and paved the way for further research into gas sensors for safety applications.

Subsequently, Matsushita Electric Industry Company introduced a humidity sensor based on metal oxide composites, designed to measure changes in humidity at elevated temperatures. This sensor was later integrated into an electronic oven to enable automated cooking.

After the 1980s, gas and VOC sensors evolved into a mature market, focusing on the detection of flammable gases, toxic gases, oxygen levels, and volatile organic compounds. Since then, continuous research and development efforts have aimed at replacing older sensors with newer, more efficient, and competitive technologies.

1.3. Types of Gas Sensors

The primary sensing mechanism in gas sensors is based on the interaction between target gas species and the sensing material. In this process, the sensing material acts as a receptor, where adsorption or reaction of gas molecules occurs on its surface. This interaction alters the physicochemical properties of the material. The resulting change is then converted into a measurable electrical signal by the transducer, effectively transforming chemical energy into an electrical response. Depending on the receptor-transducer mechanism, these interactions lead to variations in measurable electrical parameters. Such variations can be monitored through changes in resistance, capacitance, current, potential, or optical properties of the sensing material. Based on the type of electrical signal generated, gas sensors are commonly classified into the following categories:

1.3.1. Resistive Gas Sensor

Semiconductor-based gas sensors are typically engineered using semiconducting materials, most commonly metal oxides such as WO_3, SnO_2, TiO_2, and MoO_3. In recent years, two-dimensional transition metal dichalcogenides (TMDs), including MoS_2, WS_2, $MoSe_2$, and WSe_2, have also

attracted significant attention due to their elevated surface-to-volume ratio and pronounced surface reactivity. The sensing mechanism of these materials is based on resistance variations when they interact with target gases. Typically, oxygen molecules from the ambient atmosphere adsorb onto the surface of the sensing layer and capture electrons from the conduction band, forming ionized oxygen species (O_2^-, O^-, or O^{2-}). When test gas molecules interact with these pre-adsorbed oxygen species, surface reactions occur that either release electrons back into the material or further withdraw electrons. The resulting increase or decrease in resistance depends on the semiconducting type of the sensing material (n-type or p-type) and the nature of the target gas (oxidizing or reducing). In a typical device configuration, the sensing layer is deposited onto an insulating substrate and positioned between or atop two metal electrodes (Au or Pt), enabling real-time monitoring of resistance changes, as illustrated in Fig. 1.1.

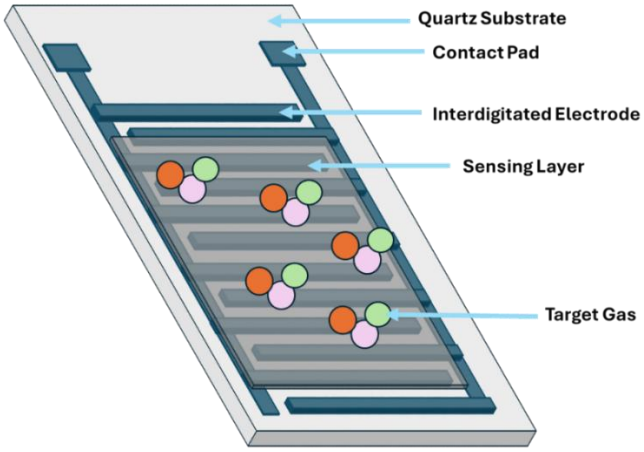


Fig. 1.1. Schematic of interdigitated electrode device used for chemiresistive based gas sensing

1.3.2. Capacitive Gas Sensor

Capacitive gas sensors function by sensing alterations in the dielectric behavior of the sensing material, especially the dielectric constant (ε). When the sensing layer is exposed to a target gas, adsorption or interaction of gas molecules alters the dielectric constant of the material. This variation in ε

leads to a corresponding variation in the capacitance of the sensor, which is measured and correlated with gas concentration. Capacitive humidity sensors are typically fabricated using hydrophilic inorganic oxides such as Ta_2O_5, Al_2O_3, and SiO_2.

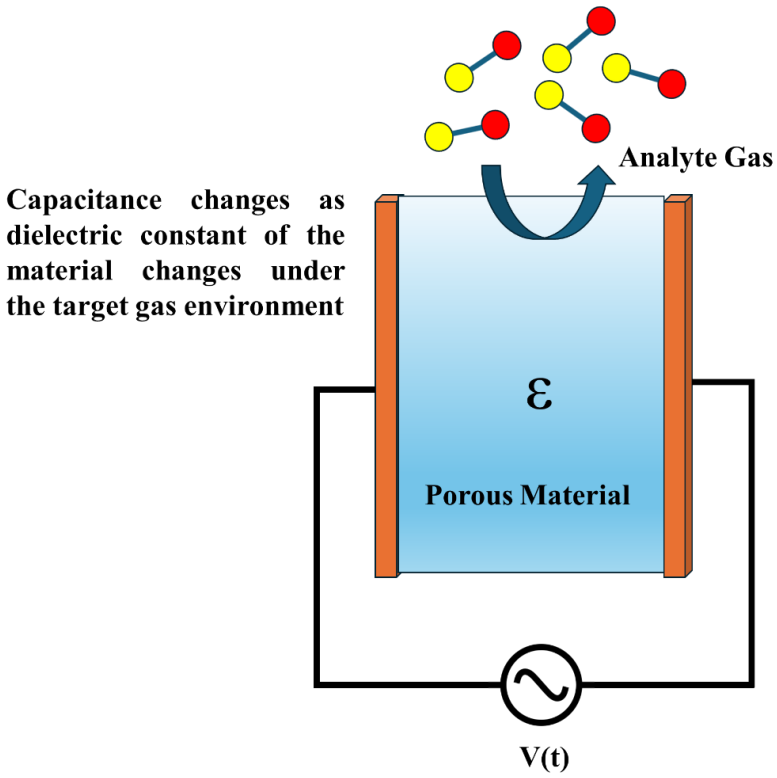


Fig. 1.2. Schematic illustration of capacitance-based gas sensor

These materials readily adsorb water molecules, resulting in a significant change in their dielectric properties with varying humidity levels. Such sensors are capable of accurately detecting humidity over a wide range of temperature and pressure conditions. Additionally, they exhibit low hysteresis, excellent long-term stability, and reliable repeatability, making them suitable for practical environmental monitoring applications. A schematic representation of the capacitive sensing mechanism is shown in Fig. 1.2.

1.3.3. Optical Gas Sensor

Optical gas sensors operate based on light propagation through an optical fiber waveguide structure. In this configuration, the conventional cladding of the optical fiber is replaced or coated with a gas-sensitive material. When the sensing layer interacts with the target gas, its optical properties change. These changes modify the conditions of light propagation within the fiber core, affecting the transmitted optical signal.

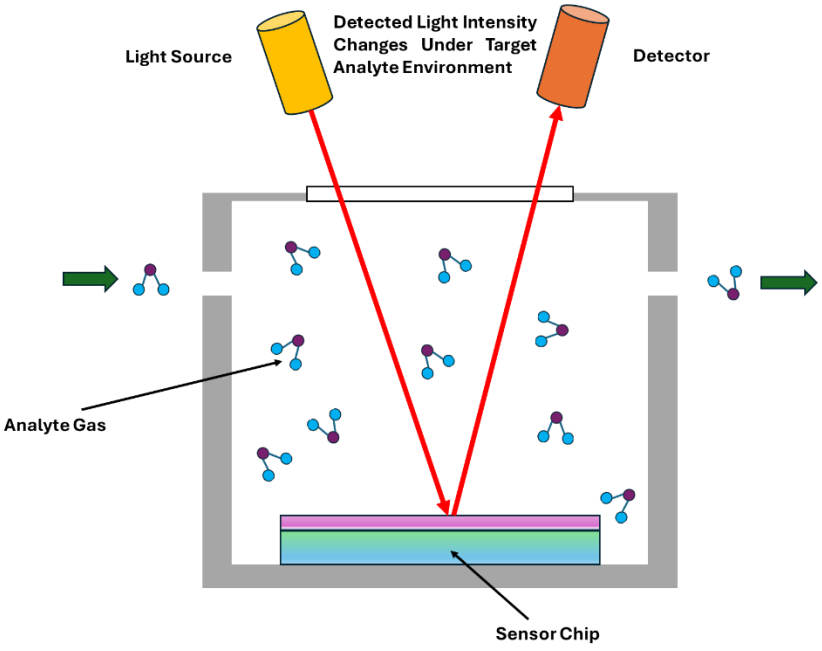


Fig. 1.3: Schematic illustration of Optical Gase Sensor

As a result, measurable variations occur in optical parameters such as phase, intensity, wavelength, and polarization of the guided light. By monitoring these changes, the presence of specific gases can be detected and their concentrations quantitatively determined. A schematic illustration of the optical fiber gas sensing mechanism is shown in Fig. 1.3.

1.3.4 Colorimetric Gas Sensor

Colorimetric gas sensors work on the principle of a visible color change that occurs when a sensing reagent or chemically active element is exposed to a target gas. This change results from a specific chemical reaction between the

gas molecules and the reagent, producing a distinct color variation that indicates the presence of the analyte. At present, colorimetric sensor tubes are widely used for the detection of various gases and VOCs. In this technique, a sealed tube containing a chemically treated reagent is exposed to an air or gas stream. The interaction between the target gas and the reagent produces a colored stain along the tube. The length of this stain is proportional to the concentration of the gas, allowing for direct quantitative estimation.

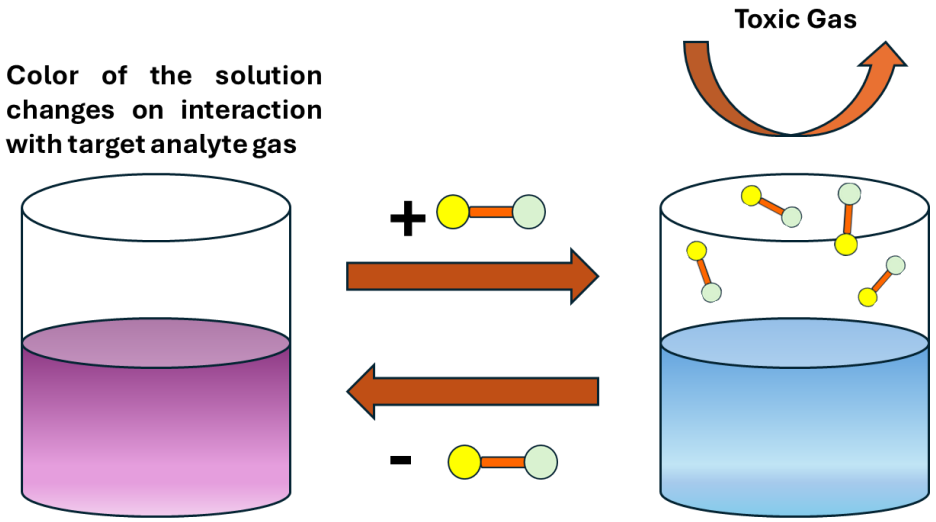


Fig. 1.4. Schematic illustration of colorimetric based gas sensor

The primary advantage of colorimetric gas detection lies in its simplicity and ease of use. These sensors are cost-effective, provide rapid response, require minimal training, and involve very low maintenance. Owing to these benefits, they represent a practical and accessible solution for on-site gas and VOC detection across industrial, environmental, and safety monitoring applications. A schematic representation of the colorimetric gas sensing mechanism is shown in Fig. 1.4.

1.3.5. Potentiometric Gas Sensor

Potentiometric gas sensors work as an electrochemical cell consisting of multiple elements: a reference electrode, a working electrode, and a solid electrolyte positioned between them. The changing concentrations of the test

gas causes the potential of the working electrode to change and the measured response signal is the potential difference between the reference electrode and the working electrode. Solid electrolytes exhibiting high ionic conductivity while acting as electronic insulators, are a crucial part of this sensor type.

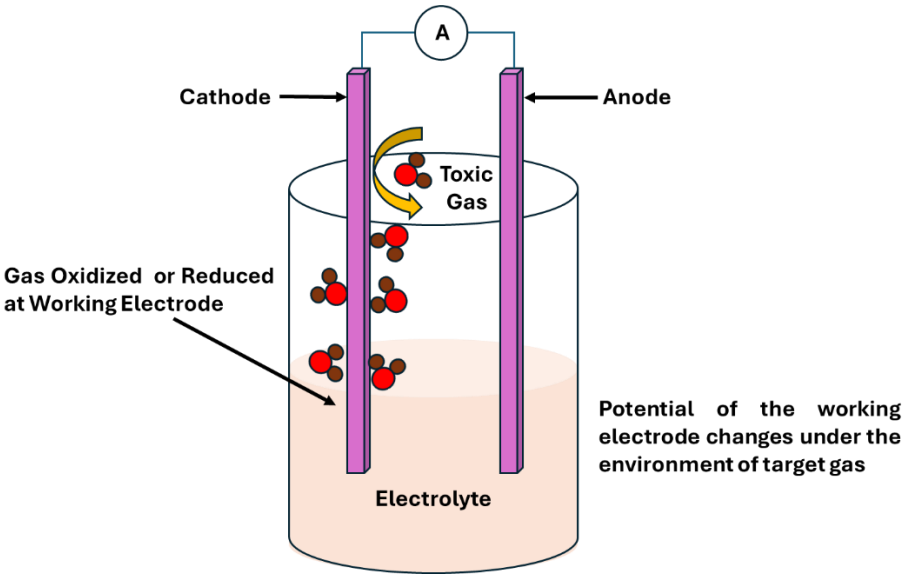


Fig. 1.5. Schematic of potentiometric gas sensor

Stabilized zirconia is one of the most advanced solid electrolytes, known for its exception oxygen ion conductivity, making it ideal for use in oxygen gas sensors. Schematic of potentiometric gas sensor is depicted in Fig. 1.5.

1.3.6. Field-Effect Transistor (FET) Gas Sensor

A gas sensor can be realized using a metal-oxide-semiconductor field-effect transistor (MOSFET) configuration. In this approach, the gas-sensitive material functions as the conductive channel between the source and drain electrodes. When the target gas interacts with the channel surface, processes such as adsorption, charge transfer, or surface reactions modify the carrier concentration and mobility within the channel. These interactions produce detectable changes in key electrical parameters of the device, including the threshold voltage and the drain-source current. The variation in these electrical characteristics serves as a direct indicator of the presence of the

target gas or VOCs, and the magnitude of the change can be correlated with gas concentration. A schematic representation of the MOSFET-based gas sensing mechanism is shown in Fig. 1.6.

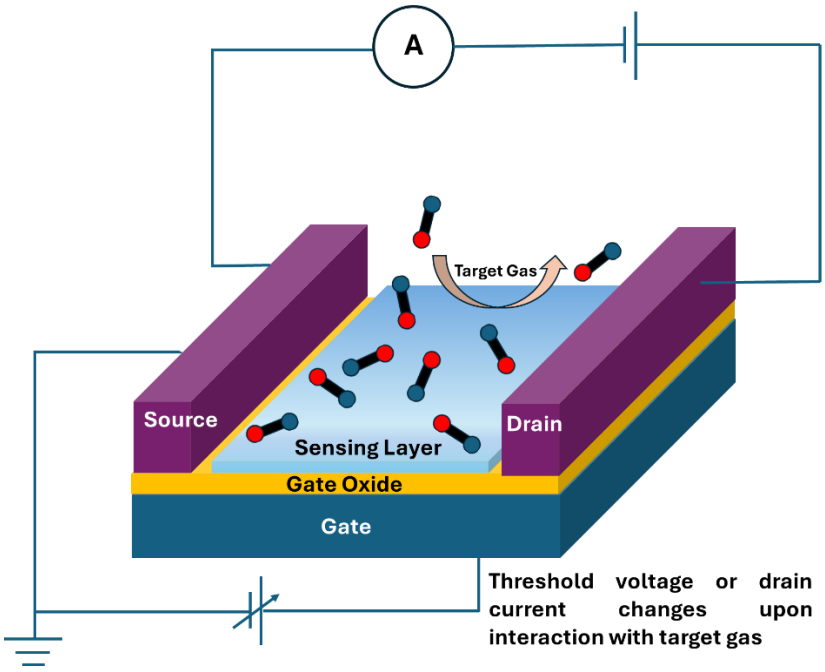


Fig. 1.6. Schematic illustration of FET based gas sensor

1.4. Gas Sensing Terminology

There are several key terms that must be clearly defined before discussing the working principles and performance of semiconductor gas sensors. These fundamental parameters form the basis for evaluating and comparing the performance of all gas sensing devices:

Response (R):

Sensor response is quantified as the ratio between the changes in the baseline resistance of the sensor when transitions from an open-air environment to a test gas under consistent operating conditions.

$$\text{Response} = \left|\frac{R_g - R_a}{R_a}\right| \times 100\% \text{ or } \frac{R_g}{R_a} \qquad (1.1)$$

Where, R_a and R_g is the electrical resistance of the sensor under open-air and test gas environments respectively.

Selectivity (S):

Selectivity is defined as the capability of a gas sensor to discriminate a specific target gas from a mixture of interfering gases, and is commonly assessed by comparing its response to various gases under identical operating conditions.

Reversibility:

Reversibility is defined as the ability of a gas sensor to restore its initial baseline state upon removal of the target gas, indicating complete recovery of its electrical characteristics following the cessation of gas–surface interactions.

Response Time (τ_{Res}):

Response time refers to the duration required for the response of a gas sensor to rise from its baseline value (0% response) to 90% of its saturated (maximum) response upon exposure to a target gas. It reflects how quickly the sensor detects the presence of the gas.

Recovery Time (τ_{Rec}):

Recovery time is defined as the time required for a gas sensor's response to decrease from its saturated (maximum) value to 10% of that value after the target gas is removed from the sensor environment. It indicates how quickly the sensor returns to its baseline state once the gas exposure ends.

Operating Temperature (T):

Operating temperature is defined as the temperature at which a gas sensor exhibits its maximum response to a target gas.

Repeatability:

Repeatability is defined as the ability of a gas sensor to consistently produce the same response when subjected to repeated cycles of exposure to a target gas followed by its removal under identical operating conditions.

Long term stability:

Long-term stability describes the capability of a gas sensor to retain its sensing performance and produce consistent responses over a prolonged period of use. It indicates that the sensitivity, baseline resistance, and overall response behavior of the sensor remain nearly unchanged despite continuous operation or repeated exposure to gases.

1.5. Semiconducting Metal Oxide (MOX) Gas Sensors

Metal oxide (MOX)-based gas sensors, typically operating on a chemiresistive principle, detect target gases through variations in the resistance of the sensing material when gas molecules adsorb onto its surface [3]. The interaction of gas molecules adsorbed on the surface with oxygen ions influences the charge carrier density, resulting in a detectable resistance change. Common MOX sensing materials include tungsten oxide (WO_3), indium oxide (In_2O_3), titanium dioxide (TiO_2), molybdenum oxide (MoO_3), manganese dioxide (MnO_2), cobalt oxide (Co_3O_4), and copper oxide (CuO). These materials are widely employed in gas sensing applications due to their cost-effectiveness, high surface-to-volume ratio, chemical and thermal stability under harsh conditions, and compatibility with silicon-based microfabrication technologies [3]. Owing to these advantageous properties, MOX-based chemiresistive sensors have become one of the most widely adopted platforms for reliable and efficient gas detection systems.

1.5.1. General Sensing Mechanism

On MOX surfaces, oxygen vacancies act as electrically and chemically active sites. Oxygen, which constitutes approximately 20.9% of atmospheric air by volume, readily interacts with these vacancy sites when the MOX surface is

exposed to air. During this interaction, oxygen molecules adsorb onto the surface and capture electrons, resulting in the formation of negatively charged oxygen species. Fig. 1.7 shows how adsorbed oxygen species interact with SnO_2 at varying temperatures. At temperatures below approximately 150 °C, the SnO_2 surface predominantly exhibits molecular ionosorption in the form of O_2^- and O_2^{2-} species. With further increase in temperature, the adsorbed oxygen species are present predominantly in atomic ionosorbed forms such as O^- and O^{2-} [4]. In n-type MOX materials, these adsorbed oxygen species create surface states that trap free electrons, leading to the formation of an electron depletion layer near the surface.

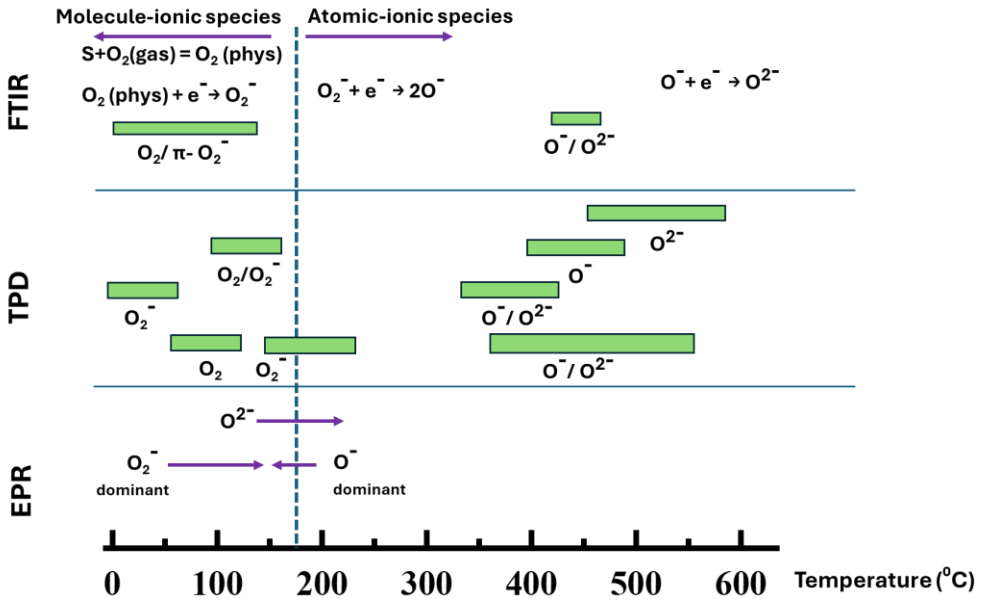


Fig. 1.7. Adsorbed oxygen species on the sensor surface at different temperatures analyzed using FTIR, TPD, and EPR techniques.

This depletion region increases the sensor resistance and plays a crucial role in the gas sensing mechanism. Furthermore, as illustrated in Fig. 1.8, the thickness of the electron depletion layer formed near the surface of an n-type MOX material varies upon the adsorption of oxygen species and significantly influences the electrical resistance of the sensing layer under different ambient conditions. An n-type MOX sensor operating under ambient

conditions is considered here for illustration. In a vacuum environment, the absence of gas species prevents oxygen adsorption on the MOX surface; consequently, no charge depletion layer is formed beneath the surface. Under these conditions, the energy bands remain nearly flat near the surface of the MOX particles. However, a very small contact or potential barrier may still exist between adjacent particles due to surface defects and interparticle contacts, as illustrated in Fig. 1.8 (a).

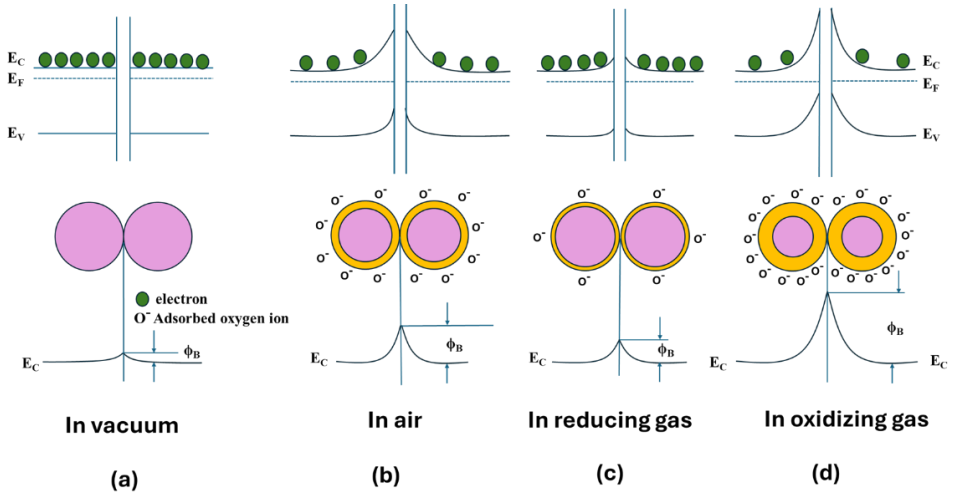


Fig. 1.8. Schematic illustration of the energy band diagram and depletion layer variation in an n-type MOX with adsorbed oxygen species under different environments: (a) vacuum, (b) air, (c) reducing gas atmosphere, and (d) oxidizing gas atmosphere

In the presence of air, oxygen molecules adsorb onto the MOX surface and capture electrons from the bulk material, leading to the formation of a charge depletion layer near the surface. The negatively charged adsorbed oxygen species and the positively charged bulk region establish an electric field at the surface, resulting in band bending, as depicted in Fig. 1.8 (b). This band bending creates a potential barrier (Φ_B) that impedes electron transport across grain boundaries and restricts particle-to-particle conduction. When the MOX surface is subjected to reducing gases such as H_2, CO, NH_3, H_2S, and CH_3OH, these gases react with the adsorbed oxygen species, releasing the trapped electrons back into the bulk. As a result, the amount of adsorbed

oxygen decreases, leading to a reduction in both the depletion layer width and the potential barrier height, as shown in Fig. 1.8 (c). Consequently, the overall resistance of the sensor decreases compared to its resistance in air. Conversely, exposure to oxidizing gases such as O_3, NO_2, and SO_2 produces an effect similar to that of oxygen in air. These gases withdraw additional electrons from the surface region, increasing the depletion layer width and potential barrier height, as illustrated in Fig. 1.8 (d), thereby giving rise to an increase in sensor resistance.

1.5.2. Factors Affecting Sensing Performance

The performance characteristics of MOX-based gas sensors are governed by numerous factors [5], [6]. Parameters such as grain size, crystallographic planes, geometry, and morphological features significantly affect gas adsorption-desorption, surface chemical reactions, and charge transport processes. Consequently, careful control and optimization of these factors are essential for improving the sensitivity, selectivity, and overall efficiency of MOX-based gas sensing devices.

1.5.2.1 Grain Size

MOX particles are typically interconnected with neighbouring particles through either grain contacts or neck contacts. In the case of grain contacts, conduction electrons must traverse a potential barrier at each grain boundary, as illustrated in Fig. 1.8(a). The overall resistance is therefore governed by the height of this potential barrier, which is strongly influenced by the surrounding atmosphere [7]. Under these conditions, the gas sensitivity is largely dependent of the metal oxide grain size.

In contrast, when neck contacts are present, conduction electrons pass through narrow conduction channels formed at the neck regions between adjacent grains, as shown in Fig. 1.8(b). The effective aperture of these necks is controlled by the surface space-charge layer [8], and the dominant contribution to the overall resistance arises from the neck resistance. Considering a three-dimensional array of uniform grains with diameter D,

connected by necks of diameter X, the neck diameter is directly proportional to the grain size and can be expressed as X = kD, where the proportionality constant k ≈ 0.8 ± 0.1.

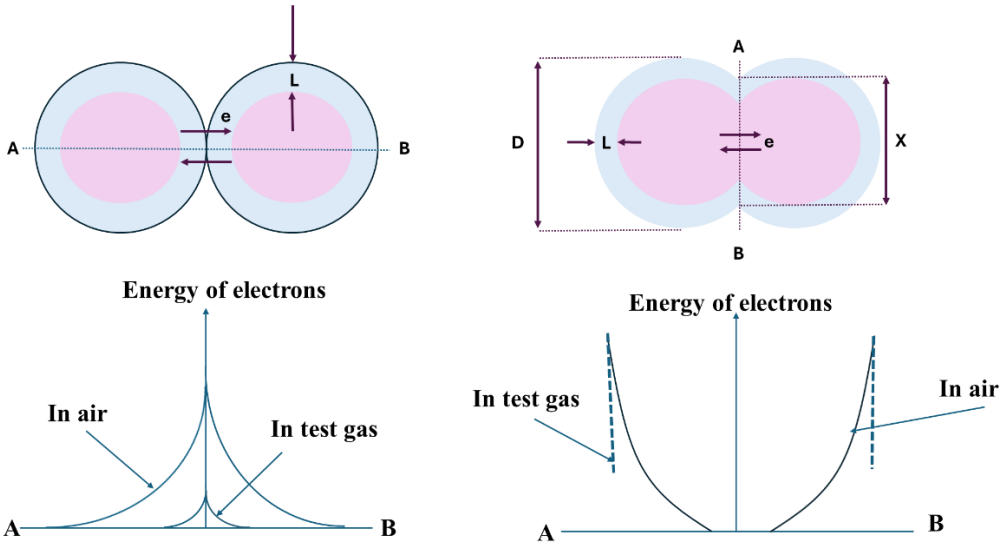


Fig. 1.9. Schematic illustration of the grain contact model and corresponding electronic band structure for (a) grain boundary contact and (b) neck contact.

Fig. 1.10 illustrates three possible conduction regimes governed by neck-controlled transport:

- **D >> 2L**: When the grain diameter is much larger than twice the depletion layer width (2L), electron conduction is dominated by grain boundary contacts. In this regime, the electrical resistance and gas sensitivity are primarily determined by grain boundary barriers.

- **D ≥ 2L**: When the grain size is comparable to twice the depletion layer width, electron transport becomes neck-controlled. In this case, sensitivity increases as the grain diameter decreases due to enhanced modulation of the conduction channel.

- **D < 2L**: When the grain diameter is smaller than twice the depletion width, the entire grain becomes depleted of charge carriers. Electron conduction is then governed by the entire grain volume.

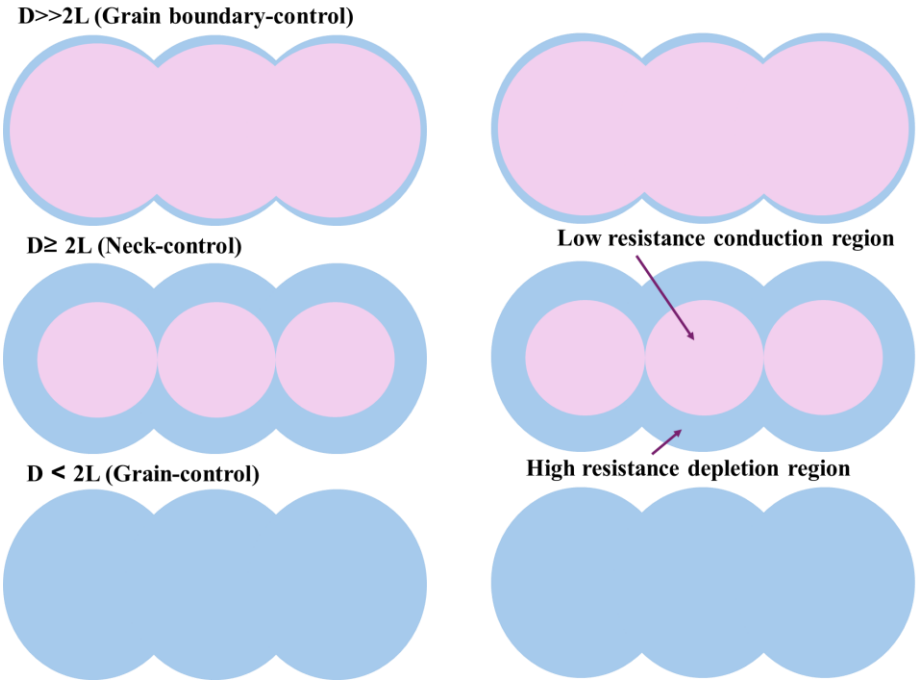


Fig. 1.10. Schematic illustration models for grain size effect

1.5.2.2 Crystallographic Plane

In the regime where **D >> 2L**, the crystallographic plane of the metal oxide plays a significant role in gas sensing performance. During the growth of MOX nanoparticles, different crystallographic planes may be exposed depending on the growth direction and synthesis conditions. These planes exhibit varying surface atomic arrangements and metal atom densities, which influence the availability of active sites for gas adsorption and surface reactions. Consequently, the specific crystallographic orientation of the exposed surfaces can strongly affect the sensing characteristics of MOX materials.

1.5.2.3. Geometrical

The geometry of MOX particles is a crucial factor affecting gas sensing performance. When the target gas interacts with the particle surface, and the reaction rate at the outer surface exceeds the diffusion rate, the gas molecules may be consumed before penetrating into the inner regions of the particles. Consequently, sensing occurs primarily at the outer active sites, while the inner sites remain largely unused. Therefore, the particle shape and the diffusion distance from the exterior surface to the interior active regions must be carefully considered during sensor design. Proper optimization of these structural features enhances gas diffusion, ensures better utilization of active sites, and improves the overall efficiency of MOX-based gas sensors.

1.5.2.4. Noble Metals Additive

Functionalization of MOX surfaces with noble metals such as Pd, Pt, and Ag is an effective strategy to enhance gas sensing performance. The incorporation of these noble metal nanoparticles improves sensitivity, selectivity, and transient response characteristics, while also lowering the optimum operating temperature of the sensor [9]. Performance enhancement arises primarily through two mechanisms: chemical sensitization and electronic sensitization [10]. In chemical sensitization, noble metals such as Pt act as catalytic activators for the target gas. They facilitate the dissociation and catalytic oxidation of gas molecules on the MOX surface, as illustrated in Fig. 1.11(a). This catalytic activity accelerates the reaction between adsorbed oxygen species and the target gas, thereby increasing the sensor response and improving sensitivity. In electronic sensitization, noble metals such as Pd and Ag form stable oxide layers (e.g., PdO and Ag_2O) in ambient air and can be readily reduced back to their metallic state when exposed to reducing gases such as H_2. Because noble metals generally possess a higher work function than MOX materials (for example, Pd compared with SnO_2), electrons tend to transfer from the MOX to the noble metal particles. Furthermore, the formation of noble metal oxides can trap additional electrons from the MOX,

leading to the development of an expanded charge depletion region within the oxide matrix, as shown in Fig. 1.11(b).

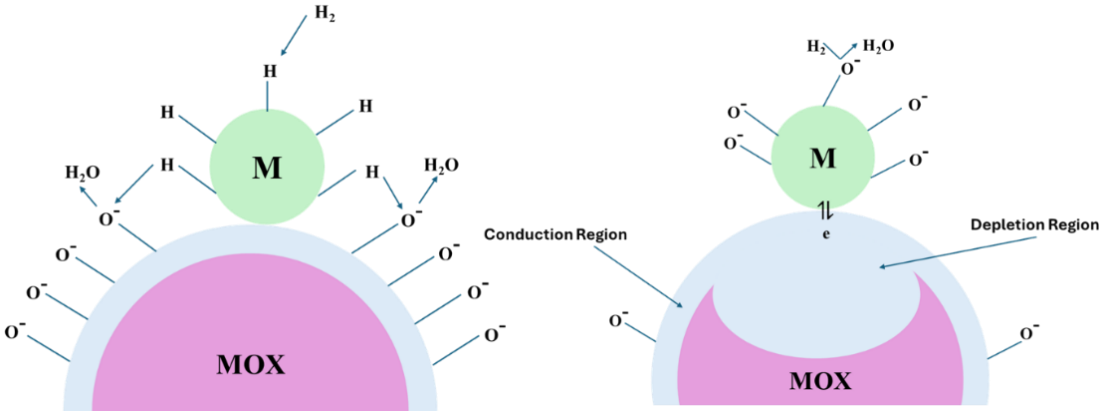


Fig. 1.11. Schematic illustration of noble metal sensitization mechanisms in MOX sensors: (a) chemical sensitization and (b) electronic sensitization.

1.5.2.5. Transition Metal Additive

Transition metal doping is an effective strategy to enhance the gas sensing performance of metal oxide nanomaterials by modifying their structural and electronic properties. The incorporation of dopants such as Ni, Cu, and Mo induces lattice distortion, reduces crystallite size, and promotes the formation of heterojunctions, thereby increasing the extent of the charge depletion region and influencing charge transport. These dopants also enhance the concentration of oxygen vacancies and introduce catalytically active sites, thereby improving gas adsorption and surface reaction kinetics. In particular, transition metals can alter carrier concentration and electronic structure, leading to enhanced sensitivity and faster response. However, the sensing performance strongly depends on the dopant concentration, as excessive doping may lead to agglomeration or hinder electron transfer, ultimately reducing sensor efficiency. Therefore, optimizing the dopant level is crucial to achieve maximum sensing performance [11-13].

1.5.2.6. Surfactant Additive

Surfactants are surface-active agents widely used in material synthesis to control the growth, morphology, and dispersion of nanostructured materials. They consist of two distinct components: a hydrophilic (water-attracting) head group and a hydrophobic (water-repelling) tail. Due to this amphiphilic nature, surfactants tend to accumulate at interfaces such as solid–liquid or liquid-air boundaries, thereby reducing surface tension and influencing interfacial interactions. In nanomaterial synthesis, surfactants play a crucial role as structure-directing or capping agents, guiding the nucleation and growth processes of particles [14].

During synthesis processes such as hydrothermal or solvothermal methods, surfactants can regulate particle size, shape, and distribution by selectively adsorbing onto specific crystal facets. This controlled growth helps in preventing particle agglomeration and promotes the formation of well-defined nanostructures with higher surface area and improved structural uniformity. The presence of surfactants can also modify the surface properties of the synthesized materials, making them highly suitable for applications that demand enhanced surface activity [15].

In the context of materials used for gas sensing, surfactants are often employed to tailor the morphology and increase the availability of active sites for gas adsorption. By facilitating the formation of porous or hierarchical nanostructures, surfactants contribute to improved gas diffusion and surface reactions, ultimately enhancing the sensing performance of the material [16].

1.5.2.7. Other Factors

Although several factors influence the performance of a gas sensor, the present study focuses primarily on two key aspects, namely the porosity of the sensing material and the overall sensor configuration, which play a crucial role in determining sensor performance.

Material Porosity:

Material porosity is a critical parameter influencing sensor performance. A porous structure facilitates rapid diffusion of gas molecules throughout the sensing layer, which improves both response and recovery times. Moreover, increased porosity enhances the effective surface area, offering more active sites for gas adsorption. As a result, highly porous materials typically exhibit faster response-recovery characteristics and improved sensitivity [17].

Sensor Configuration:

The position and configuration of metal electrodes play a key role in governing the sensor response. When the metal electrodes are deposited on top of the MOX film, they primarily measure changes in surface resistance, while variations in bulk resistance remain largely undetected.

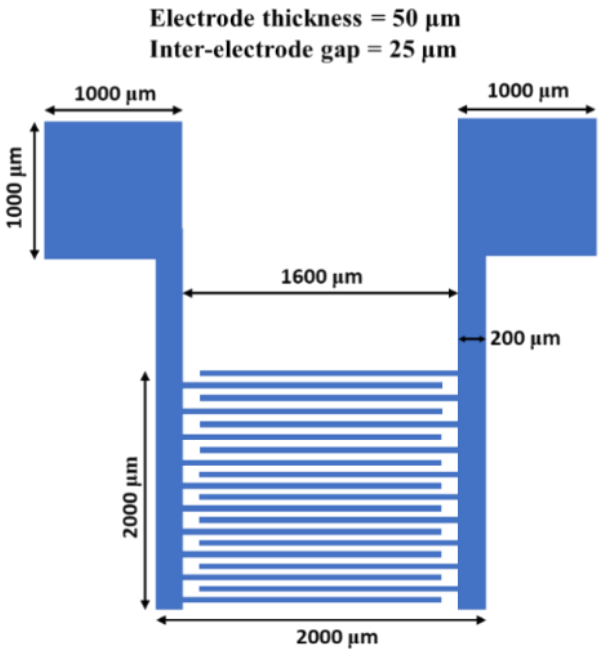


Fig. 1.12. Schematic diagram of Interdigitated Electrode Device

In contrast, electrodes positioned beneath the MOX film capture both surface and bulk resistance changes, resulting in a larger overall resistance variation

and enhanced sensitivity. In gas sensing devices, metal electrodes are commonly patterned as two contact pads or interdigitated electrodes (IDEs), as illustrated in Fig. 1.12. IDE structures are widely preferred because they increase the effective sensing area and promote gas interaction. However, parameters such as electrode thickness, spacing between adjacent electrodes, and the electrode deposition technique can significantly influence the sensing performance.

1.6. Material Selection

The selection of a suitable sensing material is a critical step in the fabrication of gas sensors. A variety of materials exhibit measurable changes in their physical or electrical properties upon exposure to target gases. Commonly used sensing materials include MOXs, two-dimensional transition metal dichalcogenides (TMDs), covalent semiconductors, polymers, and organic semiconductors. Therefore, the sensing material must be selected in accordance with the specific target gas to achieve optimal sensor performance.

1.6.1. Ideal Characteristics of a Gas Sensing Material

An ideal gas sensing material should exhibit the following characteristics [18]:

- High sensitivity toward the target gas to enable detection at low concentrations.
- Low cross-sensitivity to interfering gases, ensuring accurate and selective detection.
- Stable performance under varying humidity conditions, maintaining reliability in real-world environments.
- Long-term stability, allowing consistent sensing performance over extended periods of operation.
- Minimal baseline drift, with resistance changes primarily influenced by gas composition and temperature variations.

- Rapid adsorption kinetics, enabling quick molecular interaction of gaseous species and the sensing surface.
- Short response and recovery times, ensuring prompt detection and rapid return to baseline conditions.
- High reproducibility, providing consistent sensing behavior across repeated measurements.
- Compatibility with silicon (Si) technology, facilitating integration into microelectronic systems and sensor platforms.

1.6.2. Why Metal Oxide? and Why Cobalt Oxide (Co_3O_4)?

Metal oxide semiconductors (MOXs) are commonly chosen for gas sensing because they offer a practical balance between performance, reliability, and cost. One of their biggest advantages is their strong interaction with gas molecules-when a gas comes in contact with the surface, the material responds with a noticeable change in electrical resistance, making detection simple and effective. Their naturally high surface area provides plenty of active sites for gas adsorption, which enhances sensitivity. In addition, MOXs are chemically and thermally stable, allowing them to operate reliably even in harsh environments. Their compatibility with silicon technology also makes them easy to integrate into modern electronic devices, which further supports their widespread use in gas sensing applications.

Various semiconducting metal oxide materials are employed in gas sensing applications and can be broadly classified into three categories: pre-transition, transition, and post-transition metal oxides.

- **Pre-transition metal oxides:** These oxides are generally chemically inert and do not readily undergo oxidation-reduction reactions. Due to this limited reactivity, they are less suitable for gas sensing applications, particularly in resistive-type sensors where sensing relies on changes in electrical conductivity.

- **Transition metal oxides:** Transition metal oxides exhibit higher chemical reactivity and are widely used in gas sensing. Their electrical conductivity can change significantly upon exposure to target gases, making them well suited for chemiresistive sensing mechanisms.
- **Post-transition metal oxides:** Post-transition metal oxides are also commonly utilized in gas sensing applications. They respond to variations in gas composition by exhibiting measurable changes in their electrical properties.

Since the 1960s, numerous metal oxides have been extensively investigated and applied in gas sensing, including ZnO, SnO_2, TiO_2, WO_3, MoO_3, In_2O_3, Co_3O_4, CuO and NiO.

Structure and Phases of Co_3O_4:

Cobalt (II, III) oxide (Co_3O_4) crystallizes in a normal cubic spinel structure, where oxide ions form a face-centered cubic (fcc) lattice. Within this framework, Co^{2+} ions occupy one-eighth of the tetrahedral interstitial sites, while Co^{3+} ions reside in half of the octahedral sites. The coexistence of Co^{2+} and Co^{3+} ions provide a reversible redox couple (Co^{2+}/Co^{3+}), which contributes to the versatile functional properties of Co_3O_4 and makes it suitable for applications such as heterogeneous catalysis, electrochemical systems, and gas sensing [19]. Nanostructured forms of Co_3O_4, including nanoporous architectures, offer significant advantages due to their high surface-to-volume ratio and enhanced accessibility to gas- and liquid-phase species. These features promote efficient surface reactions and improve functional performance. In particular, nanostructured Co_3O_4 has demonstrated excellent catalytic activity for low-temperature CO oxidation and exhibits strong catalytic efficiency in various surface-driven reactions, highlighting its potential for sensing and catalytic applications [20-21].

Electronic and Optical Properties:

The electrical and optical properties of Co_3O_4 are strongly influenced by its crystalline structure and defect chemistry. Co_3O_4 is a p-type semiconductor whose electrical conductivity is primarily governed by hole transport arising from the mixed valence states of Co^{2+} and Co^{3+} ions. At room temperature, Co_3O_4 exhibits an optical band gap typically in the range of 1.6-2.2 eV, depending on synthesis conditions and nanostructure, which enables absorption in the visible region. The spinel crystal structure of Co_3O_4 is prone to intrinsic defects, among which oxygen vacancies are the most significant. Oxygen vacancies arise when oxygen atoms are missing from their lattice sites, altering the local charge balance. From an electronic perspective, these vacancies modify the charge distribution around neighbouring cobalt ions and can influence carrier concentration and mobility. Such defect states introduce energy levels within the band structure and play an important role in determining the electrical conductivity, catalytic activity, and gas sensing behaviour of Co_3O_4. Both pristine and doped Co_3O_4 have demonstrated significant potential for gas sensing applications. Various nanostructured forms of Co_3O_4 exhibit enhanced catalytic activity owing to the reversible redox behaviour of the Co^{2+}/Co^{3+} couple, which promotes efficient surface reactions and gas adsorption. As a p-type semiconductor, Co_3O_4 shows an increase in resistance upon exposure to reducing gases and a decrease in resistance in the presence of oxidizing gases [22]. Both pure Co_3O_4 and doped Co_3O_4 (e.g., In-, Ga-, or Sn/Mn-doped) have shown excellent sensitivity toward gases such as carbon monoxide, hydrogen, hydrogen sulphide, and nitrogen oxides over a wide temperature range. Doping further enhances catalytic activity, lowers operating temperature, and improves selectivity, making Co_3O_4-based materials highly promising for advanced gas sensing applications. [23-25]

Table 1.1. Pristine and functionalized, doped Co3O4 gas sensor.

Material	Gas	T_{opt} (°C)	Conc. (ppm)	Response (%)	τ_{Res}/τ_{Rec}(sec)	Ref.
ZnO nanoflower grown on Co_3O_4	CO	210°C	100	38	38/50	[26]
Mn doped Co_3O_4	CO	125°C	40	280	12/26	[27]
NiO functionalized Co_3O_4 hetero-nanocomposite	CO	150°C	300	150	NA	[28]
Mesoporous Co_3O_4	CO	200°C	25	210	NA	[29]
PANI/Co_3O_4 nanocomposite	CO	RT	75	81	40/140	[30]

1.7. Main Aim and Objectives

The main aim of this thesis is to improve the sensitivity and selectivity of three-dimensional (3D) pristine and metal-functionalized Co_3O_4 for the detection of carbon monoxide (CO) and the volatile organic compound (VOC) methanol. To fulfill this overall objective, the following specific goals are systematically addressed in this study:

- To synthesize the active sensing layer based on pristine and metal-doped Co_3O_4 using facile hydrothermal technique. Subsequently, gas sensor devices are fabricated by integrating the prepared sensing material onto suitable substrates with patterned electrodes.
- To systematically examine the morphological, structural, and compositional characteristics of the synthesized Co_3O_4 using advanced material characterization techniques such as FESEM, EDX, XPS, XRD, and BET surface area analysis.
- To investigate the gas sensing performance of the fabricated sensors toward CO and methanol using an indigenously developed gas sensing setup. The sensing studies include evaluation of sensitivity, selectivity, repeatability, and long-term stability. Furthermore, the

effects of operating temperature, gas concentration, and ambient humidity on the sensing behaviour are comprehensively analyzed.

1.8. Thesis Organization

The research presented in this thesis provides a comprehensive investigation of the hydrothermal synthesis of cobalt oxide-based sensing materials and their application in gas detection. In addition, the study systematically evaluates the sensing performance of the synthesized materials under varying environmental conditions. The thesis is organized into five chapters, structured as follows:

Chapter 1 presents a concise review of the existing literature, covering the fundamentals of gas sensing, various types of gas and VOC sensors, and key sensing parameters. It discusses MOXs as gas sensing materials and outlines different strategies for enhancing sensitivity and selectivity. The chapter also introduces Co_3O_4 as the primary sensing material and reviews previously reported Co_3O_4-based gas sensors.

Chapter 2 focuses on the fabrication of the gas sensor devices and the evaluation of their performance. It details the material characterization techniques employed to analyze the crystallinity, morphology, and surface properties of the sensing layer. These techniques include structural and microscopic analyses to understand the material properties. Furthermore, the chapter describes the design and operation of a customized dynamic flow gas sensing setup used to assess the sensing characteristics of the fabricated devices.

Chapter 3 describes a novel and facile hydrothermal synthesis method for the preparation of pristine Co_3O_4 and Mo-doped Co_3O_4 with varying molybdenum concentrations. The CTAB-assisted Mo-doped Co_3O_4 sensor demonstrated enhanced sensitivity and a strong response toward carbon monoxide (CO) gas.

Chapter 4 presents the analysis of commercial CO sensor (MQ7) with the CTAB-assisted Mo-doped Co_3O_4 sensor.

Chapter 5 summarizes the key findings of the research and discusses potential directions for future work, highlighting opportunities for further improvement and application of Co_3O_4-based gas sensing materials.

1.9. References

[1] W. Weppner, "Solid-state electrochemical gas sensors", Sens. and Actuators, vol. 12, no. 2, pp. 107–119, 1987.

[2] T. Seiyama, A. Kato, K. Fujiishi, and M. Nagatani, "A New Detector for Gaseous Components Using Semiconductive Thin Films", Anal. Chem., vol. 34, no. 11, pp. 1502–1503, 1962.

[3] N. Barsan, D. Koziej, and U. Weimar, "Metal oxide-based gas sensor research: How to?", Sens. Actuators B Chem., vol. 121, no. 1, pp. 18-35, 2007.

[4] C. Patel, B. Mandal, R.G. Jadhav, T. Ghosh, M. Dubey, A.K. Das, M.T. Htay, V.V. Atuchin, and S. Mukherjee, "S, N co doped carbon dot-functionalized WO_3 nanostructures for NO_2 and H_2S detection", ACS Appl. Nano Mater., vol. 5, no. 2, pp. 2492-2500, 2022.

[5] N. Yamazoe, Y. Kurokawa, and T. Seiyama, "Effects of additives on semiconductor gas sensors", Sens. and Actuators, vol. 4, pp. 283–289, 1983.

[6] G. Heiland, "Homogeneous semiconducting gas sensors", Sens. and Actuators B: Chem., vol. 2, pp. 343–361, 1982.

[7] H. Ihokura, "SnO_2-based inflammable gas sensors", 1983.

[8] H. Mitsudo, "Ceramics for gas and humidity sensors (part I) gas sensor", Ceramics, vol. 15, pp. 339-345, 1980.

[9] N. Yamazoe, Y. Kurokawa, and T. Seiyama, “Effects of additives on semiconductor gas sensors”, Sens. and Actuators, vol. 4, pp. 283-289, Jan. 1983.

[10] L.Y. Zhu, L.X. Ou, L.W. Mao, X.Y. Wu, Y.P. Liu, and H.L. Lu, “Advances in Noble Metal-Decorated Metal Oxide Nanomaterials for Chemiresistive Gas Sensors: Overview”, Nanomicro Lett, vol. 15, no. 1, pp. 89, 2023.

[11] C.N. Wang et al. "Advances in doped ZnO nanostructures for gas sensor." The Chemical Record, vol. 20, no. 12, pp. 1553-1567, 2020.

[12] P.S. Kolhe et al. "Effect of Cu doping concentration on H_2S gas-sensing properties of Cu-doped SnO_2 thin films." Applied Physics A, vol. 125, no. 5, pp. 372, 2019.

[13] Z. Lin et al. "The effect of Ni doping concentration on the gas sensing properties of Ni doped SnO_2." Sensors and Actuators B: Chemical, vol. 239, pp. 501-510, 2017.

[14] W. Wei et al. "Surfactant-assisted cooperative self-assembly of nanoparticles into active nanostructures." IScience, vol. 11, pp. 272-293, 2019.

[15] A.P. Patil et al. "Surfactant-assisted tungsten oxide for enhanced acetone sensing and solar-driven photocatalysis: exploring the role of surfactants." RSC advances, vol. 15, no. 34, pp. 27895-27907, 2025.

[16] J. Jasmin et al. "Synthesis, analysis and characterization of surfactant-assisted TiO_2 nanoparticles for ammonia gas sensor applications." Ceramics International, vol. 50, no. 24, pp. 52262-52269, 2024.

[17] R. W. J. Scott et al. “Tin Dioxide Opals and Inverted Opals: Near-Ideal Microstructures for Gas Sensors”, Adv. Mater., vol. 13, no. 19, pp. 1468-1472, Sep. 2001.

[18] G. Korotcenkov, “Metal oxides for solid-state gas sensors: What determines our choice?”, Mater. Sci. Eng. B, vol. 139, no. 1, pp. 1-23, Apr. 2007.

[19] T. Baidya et al. "Ultra-low-temperature CO oxidation activity of octahedral site cobalt species in Co_3O_4 based catalysts: unravelling the origin of the unique catalytic property." The Journal of Physical Chemistry C, vol. 123, no. 32, pp. 19557-19571, 2019.

[20] T. Sen et al. "Room temperature CO sensing by polyaniline/Co_3O_4 nanocomposite." Journal of Applied Polymer Science, vol. 133, no. 42, 2016.

[21] D. Patil et al. "Highly sensitive and fast responding CO sensor based on Co_3O_4 nanorods." Talanta, vol. 81, no.1-2, pp. 37-43, 2010.

[22] J. M. Xu and J. P. Cheng. "The advances of Co_3O_4 as gas sensing materials: A review." Journal of Alloys and Compounds, vol. 686, pp. 753-768, 2016.

[23] J. Wu et al. "Extremely sensitive and accurate H_2S sensor at room temperature fabricated with In-doped Co_3O_4 porous nanosheets." Dalton transactions, vol. 48, no. 22, pp. 7720-7727, 2019.

[24] C. Qin et al. "Enhancing the surface activity of Co_3O_4 by gallium doping to increase the sensitivity of conductometric CO gas sensors." Sensors and Actuators B: Chemical vol. 429, pp. 137288, 2025.

[25] C. Qin et al. "Sn and Mn co-doping synergistically promotes the sensing properties of Co_3O_4 sensor for high-sensitive CO detection." Sensors and Actuators B: Chemical, vol. 390, pp. 133930, 2023.

[26] M Chen, et al. "MOF-derived Co_3O_4 nanoparticles over direct grown ZnO nanoflower on ceramic for CO sensor with high selectivity." Sensors and Actuators B: Chemical, vol. 401, pp.134951, 2024.

[27] C. Qin et al. "Metal-organic frameworks-derived Mn-doped Co_3O_4 porous nanosheets and enhanced CO sensing performance." Sensors and Actuators B: Chemical, vol. 351, pp. 130943,2022.

[28] K.W. Chen et al. "NiO functionalized Co_3O_4 hetero-nanocomposites with a novel apple-like architecture for CO gas sensing applications." Materials Letters, vol. 255, pp. 126508, 2019.

[29] S. Vetter et al. "Nanostructured Co_3O_4 as a CO gas sensor: temperature-dependent behavior." Sensors and Actuators B: Chemical, vol. 206 , pp. 133-138, 2015.

[30] T Sen et al. "Room temperature CO sensing by polyaniline/Co_3O_4 nanocomposite." Journal of Applied Polymer Science, vol.133, no.42, 2016.

Chapter 2
Material Synthesis and Characterization for Gas Sensor Development

2.1 Introduction

The rapid advancement of nanotechnology, coupled with the relentless drive toward miniaturization of electronic and sensing devices, has significantly increased the demand for engineered nanomaterials with precisely controlled size, morphology, surface characteristics, and tunable electronic, optical, and catalytic properties [1]. These distinctive characteristics make them highly promising for the development of advanced technologies and a wide range of potential applications. Nanomaterials can be deposited through a variety of physical and chemical deposition techniques, each offering specific advantages and limitations depending on the intended application and material requirements. However, chemical deposition methods are generally more cost-effective and simpler to implement compared to physical deposition techniques. In this thesis, nanostructured materials have been synthesized using chemical routes, with primary emphasis on the hydrothermal method The synthesized samples were systematically characterized using various analytical techniques. The surface morphology and microstructural features were examined using Field Emission Scanning Electron Microscopy (FESEM), while the crystalline structure and phase purity were analyzed through X-ray Diffraction (XRD). The elemental composition and chemical states of the constituent elements were investigated using Energy Dispersive X-ray Spectroscopy (EDX) and X-ray Photoelectron Spectroscopy (XPS). Furthermore, the specific surface area of the nanostructured materials was determined using the Brunauer-Emmett-Teller (BET) method due to its simplicity, cost-effectiveness. All synthesized materials were drop-casted onto suitable interdigitated electrode devices with substrates such as glass, SiO_2/Si, or PDMS, depending on the device requirements. The interdigitated electrodes (IDEs) were fabricated via photolithography on the insulating substrate to complete the device

architecture. Subsequently, the gas sensing performance of the fabricated devices was evaluated toward different gases at various concentrations. A detailed description of material synthesis techniques, material characterization methods, and the gas sensing measurement setup is provided in the following section.

2.2 Synthesis Tools

In this thesis, nanostructured materials were synthesized through chemical deposition routes, predominantly utilizing the hydrothermal technique. Specifically, a simple and efficient hydrothermal method was adopted to synthesize CTAB-assisted Mo-doped Co_3O_4, which functions as the active sensing layer in the fabricated gas sensor devices.

2.2.1. Hydrothermal Synthesis

The term 'hydrothermal' was first introduced in the 19th century by British geologist Sir Roderick Murchison to describe geological processes responsible for the formation of rocks and minerals within the Earth's crust under high-temperature and high-pressure aqueous conditions [2]. Subsequent advancements in hydrothermal synthesis further demonstrated its potential for controlled crystal growth. In 1946, Nacken successfully achieved the hydrothermal growth of a large single crystal of quartz, representing a significant milestone in the evolution of this technique [2]. Shortly thereafter, in 1948, Barrer synthesized single-crystalline zeolites using the hydrothermal method, thereby reinforcing its effectiveness and reliability for the preparation of well-defined crystalline materials. Since its early development, hydrothermal synthesis has become a versatile and cost-effective method widely used in materials science and solid-state chemistry for the controlled growth of nanostructured materials with unique functional properties.

2.2.1.1 Principle

The hydrothermal process involves a physicochemical reaction and crystallization mechanism carried out in an aqueous medium at temperatures and pressures typically exceeding 100°C and 0.1 MPa, respectively [3]. This

method utilizes the intrinsic properties of water, such as density, dielectric constant, and ionic conductivity, which vary significantly with temperature and pressure. Consequently, the solvent characteristics of water are altered under hydrothermal conditions. At ambient conditions, water has a high dielectric constant (~78), enabling it to effectively dissolve ionic and polar species [4]. However, with increasing temperature, the dielectric constant decreases markedly, thereby modifying its solubility behavior and enhancing its ability to interact with non-polar or organic species.

The hydrothermal synthesis process generally involves two fundamental stages: crystal nucleation and subsequent crystal growth. At elevated temperatures, the formation of a supersaturated solution enhances the nucleation rate, thereby facilitating the generation of stable nuclei. The critical radius of the nuclei is inversely proportional to the degree of supersaturation, meaning that higher supersaturation levels favour the formation of smaller nuclei. The subsequent crystal growth stage is commonly explained by the Ostwald ripening mechanism, in which smaller crystallites dissolve and redeposit onto larger ones, leading to the growth of thermodynamically stable particles. To overcome the nucleation energy barrier, sufficient external or thermal energy is required, which is supplied under the elevated temperature conditions of the hydrothermal process. The hydrothermal method has been widely employed in various areas of materials research due to its versatility and effectiveness. Its key applications include:

- Growth of high-quality single crystals.
- Synthesis of nanostructured materials with well-defined and controlled morphologies.
- Stabilization and preparation of novel or metastable compounds.
- Surface modification, decomposition, etching, and corrosion-related processes.

Compared to other chemical and physical deposition techniques, the hydrothermal method offers several distinct advantages:

- It is relatively simple to implement and cost-effective.
- Nanomaterials can be directly synthesized from solution without requiring complex post-processing steps.
- Particle size can be effectively tuned by adjusting reaction parameters such as temperature and duration.
- Morphology and shape of the particles can be controlled through careful selection of precursor materials and reaction conditions.
- The chemical composition and stoichiometry can be precisely regulated, making the method particularly suitable for synthesizing metastable materials.

2.2.1.2. Instrumentation

Hydrothermal synthesis is carried out in a sealed reaction vessel (autoclave), where the internal pressure is governed by the applied temperature and the filling fraction of the solution. As the temperature increases, the vapor pressure inside the vessel rises accordingly, creating the high-pressure environment necessary for crystal formation. Effective crystal growth occurs only when the vessel is filled beyond a critical level, typically above 32% of its total volume, with optimal growth generally observed when the filling fraction exceeds approximately 65% [5]. The standard reactor used for hydrothermal synthesis is an autoclave, which serves as a sealed high-pressure reaction chamber. The first autoclave was developed in Europe during the 19th century and was subsequently adopted worldwide in the 20th century for various chemical and materials processing applications. An ideal autoclave designed for hydrothermal synthesis should possess the following characteristics:

- Chemical inertness toward acids, bases, and oxidizing agents to prevent contamination or corrosion.

- Operational simplicity and ease of handling.
- Appropriate shape and size to ensure a uniform temperature distribution within the reaction medium.
- High mechanical strength with a leak-proof design to safely withstand elevated temperatures and pressures generated during the reaction.

Stainless steel is the most commonly used material for the fabrication of autoclaves due to its high mechanical strength and excellent resistance to corrosion. However, the solvents and chemical reagents employed in hydrothermal reactions are often highly corrosive, particularly under elevated temperature and pressure conditions. Prolonged exposure to such harsh environments may lead to degradation of the vessel material. To prevent corrosion and contamination, an inner liner is typically introduced inside the stainless-steel autoclave.



Fig. 2.1. Teflon-lined stainless-steel autoclave used in this thesis work.

This inner lining must be chemically inert toward the reaction medium. Polytetrafluoroethylene (PTFE), commonly known as Teflon, is widely used

for this purpose because of its excellent chemical resistance. The Teflon liner (or beaker) is placed inside the stainless-steel autoclave with minimal or no empty space to ensure safe and efficient operation. However, it is important to note that the maximum operating temperature of a Teflon liner is generally limited to approximately 300 °C. The Teflon-lined stainless-steel autoclave utilized in this thesis work is illustrated in Fig. 2.1.

2.2.1.3. Operations

A stainless-steel autoclave equipped with a Teflon liner is commonly employed for carrying out hydrothermal synthesis. Prior to the reaction, a homogeneous precursor solution is prepared separately in a suitable container, typically a glass beaker. A measured quantity of solvent, generally deionized water, is taken and maintained under continuous magnetic stirring at room temperature to ensure uniform mixing. Subsequently, the required precursors are introduced into the solvent and stirred continuously until complete dissolution is achieved. Depending on the synthesis requirements, the pH of the solution may be adjusted by adding an appropriate acid or base, followed by further stirring to ensure homogeneity. If necessary, additives or surfactants are incorporated at this stage to influence nucleation and growth behavior. The prepared solution is then carefully transferred into the Teflon liner, which is subsequently sealed within the stainless-steel autoclave. The filling volume is typically maintained above a certain fraction of the total capacity to facilitate sufficient pressure development during the reaction. The sealed autoclave is then placed inside a thermal oven and heated to a temperature generally above 100 °C for a specified duration ranging from several hours to days, depending on the desired synthesis conditions [3]. Upon completion of the reaction, the autoclave is removed from the oven and allowed to cool naturally to room temperature. The resulting product is then collected, typically by filtration or centrifugation, and washed multiple times with suitable solvents to remove any residual impurities. Finally, the purified material is dried and, if required, further treated (e.g., calcination) to obtain

the desired phase and crystallinity. The overall flow chart of the hydrothermal synthesis process is presented in Fig. 2.2.

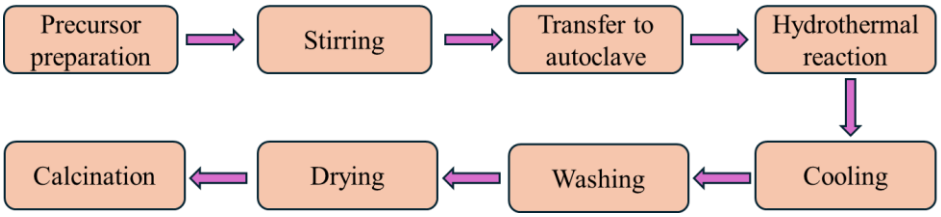


Fig. 2.2. Flowchart of hydrothermal synthesis

2.3. Sensing Layer Characterization Techniques

To systematically investigate the morphology-dependent gas and VOC sensing properties of the synthesized nanomaterials, it is essential to first conduct comprehensive material characterization. Prior to evaluating their potential device applications, the structural, surface, phase, and elemental characteristics of the active layer were thoroughly examined using various advanced characterization techniques. These analyses provide critical insights into the crystal structure, surface morphology, and compositional properties of the materials, which directly influence their sensing performance. The specific characterization techniques employed in this thesis are discussed in the following sections.

2.3.1. X-Ray Diffraction Instrument

X-ray diffraction (XRD) is a powerful and widely used characterization technique for analyzing the structural properties of materials. It provides detailed information regarding lattice parameters, crystal structure, phase identification, crystallographic orientation, strain, and average crystallite size. The fundamental components of an XRD system include an X-ray source for generating monochromatic radiation, a sample holder where the material is positioned, and an X-ray detector that records the diffracted X-rays emerging from the sample.

X-rays are generated when high-energy charged particles, such as electrons, strike a target material (commonly copper). During this interaction, the energetic electrons lose a portion of their kinetic energy, which is subsequently emitted in the form of electromagnetic radiation known as X-rays. X-rays are a form of electromagnetic radiation with wavelengths typically ranging from 0.01 to 100 Å. In X-ray diffraction analysis, monochromatic X-rays with wavelengths close to ~1 Å are generally used, as this wavelength is comparable to the interatomic spacing in crystalline materials, enabling effective diffraction from crystal planes.

In X-ray diffraction (XRD), a parallel beam of monochromatic X-rays is directed onto the sample surface. When the incident X-rays interact with the crystalline planes of the material, they are diffracted according to **Bragg's law**, which describes the condition for constructive interference of the diffracted waves. Bragg's law is expressed as: $n\lambda=2d\sin\theta$ (2.1) where:

- **λ** represents the wavelength of the incident X-ray radiation.
- **d** denotes the interplanar spacing between the atomic planes in the crystalline structure.
- **θ** is the angle between the incident X-ray beam and the crystal planes.
- **n** is an integer corresponding to the order of diffraction (order of interference).

The intensity of the diffracted X-rays is recorded as a function of the diffraction angle (2θ), and the obtained diffraction pattern is subsequently analyzed to determine the crystal orientation of the sample. In crystalline solids, atoms are arranged in an ordered and periodic arrangement known as a lattice. The characteristic interatomic spacing and interactions within this lattice give rise to a unique XRD pattern for each material [6]. Consequently,

the diffraction pattern can be used to identify the crystal structure of the material.



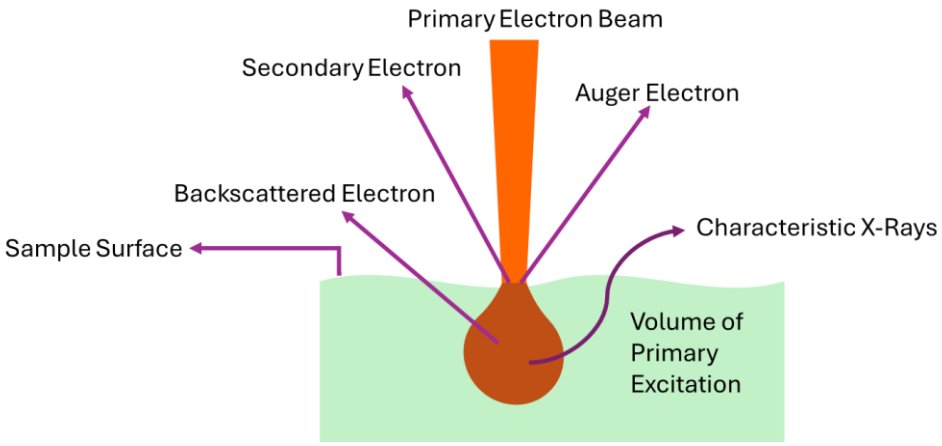
Fig. 2.3. Photographic image of the Rigaku SmartLab Automated Multipurpose X-ray Diffractometer.

The positions of the diffraction peaks along with their corresponding intensities provide valuable information regarding the structural characteristics of the sample. In this thesis, X-ray diffraction (XRD) analysis of the synthesized and deposited materials is carried out using a Rigaku SmartLab Automated Multipurpose X-ray Diffractometer. Fig. 2.3 presents the actual photograph of the Rigaku X-ray diffractometer utilized in this study.

2.3.2. Field Emission Scanning Electron Microscopy (FESEM) and Energy Dispersive X-ray (EDX) Spectroscopy

Field Emission Scanning Electron Microscopy (FESEM) is a widely used technique for obtaining high-resolution images of the surface morphology of solid materials. In this method, the sample surface is scanned in a raster

pattern using a focused beam of high-energy electrons. The main components of a FESEM system include a field emission electron gun, a set of electromagnetic lenses, an electron detection system, and a display unit such as cathode-ray tubes (CRTs) or digital imaging systems. In FESEM, electrons are generated from a field emission gun and subsequently accelerated and focused by a series of electromagnetic lenses toward the sample surface within a high-vacuum chamber. The incident electrons typically possess energies in the range of 0.5-30 keV. When these high-energy electrons interact with the surface of the solid sample, they lose energy through various interactions, leading to several types of emitted signals.



Fig, 2.4. Schematic illustration of the interaction between the incident electron beam and the sample surface.

These signals include secondary electrons, backscattered electrons, X-rays or photons, Auger electrons, cathodoluminescence (visible light), elastically scattered electrons, inelastically scattered electrons, unscattered electrons, and heat. Among these emitted signals, secondary electrons and backscattered electrons play a crucial role in image formation in FESEM. The interaction between the incident electron beam and the sample surface is illustrated schematically in Fig. 2.4. Secondary electrons are electrons emitted from the near-surface region of the sample, typically within a depth of about 0-10 nm. These electrons originate from the outer shells of the atoms and possess

relatively low binding energy with the nucleus. When the sample surface is bombarded with high-energy incident electrons, sufficient energy is transferred to these loosely bound electrons, enabling them to escape from the surface. The energy of secondary electrons generally lies in the range of 0-50 eV, with most of them having energies between 3 and 5 eV. Because they are generated very close to the surface, secondary electrons are primarily responsible for providing detailed information about the surface morphology and topography of the sample.

Backscattered electrons, on the other hand, are incident electrons that are elastically scattered by the atoms of the sample and redirected out of the material. These electrons retain a large fraction of the incident beam energy, typically close to three-fourths of the original electron energy. The number of backscattered electrons produced is strongly dependent on the atomic number of the elements present in the sample; materials with higher atomic numbers tend to generate a greater number of backscattered electrons. As a result, backscattered electrons provide compositional contrast in FESEM images and offer information related to atomic number differences and subsurface features within the sample. In addition to these signals, characteristic X-rays can also be generated when the high-energy incident electron beam removes an electron from the inner (core) shell of an atom in the sample. The resulting vacancy is quickly filled by an electron from a higher energy shell, and the energy difference between these shells is released in the form of electromagnetic radiation, typically as X-rays. The energy of these emitted X-rays is unique to each element, making them useful for elemental identification and compositional analysis.

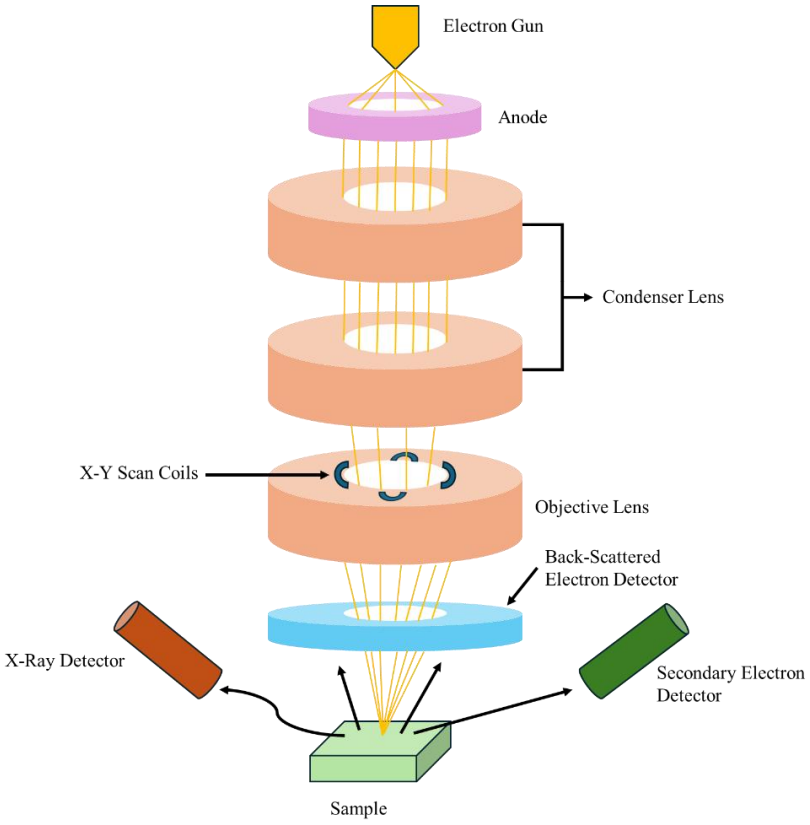


Fig. 2.5. Schematic illustration of the FESEM–EDX working principle

The analysis of the energy of the emitted X-rays is carried out using Energy Dispersive X-ray (EDX) spectroscopy. This technique is widely used for determining the elemental composition of materials. An EDX system generally consists of four main components: an electron beam source, an X-ray detector, a pulse processor, and an analyzer. In this system, the detector captures the emitted X-rays and converts them into corresponding electrical voltage signals. These signals are then transmitted to the pulse processor, where the voltage pulses are processed and quantified. Finally, the processed signals are sent to the analyzer, which interprets them to provide the elemental composition and quantitative analysis of the sample.



Fig. 2.6. Photograph of the GEMINI SEM 360 scanning electron microscope used for surface morphology analysis.

The schematic representation of the working principle of the FESEM-EDX system is shown in Fig. 2.5. In order to reduce the overall cost and improve efficiency, EDX systems are commonly integrated with scanning electron microscopes such as SEM or FESEM. In the present thesis work, a GEMINI SEM 360 system has been utilized for both FESEM imaging and EDX elemental analysis of the synthesized materials. An image of the GEMINI SEM 360 instrument used in this study is presented in Fig.2.6.

2.3.3. Raman Spectroscopy Instrument

Raman spectroscopy is a widely used analytical technique in materials science for studying phonons, as well as vibrational, rotational, and low-

frequency modes of materials. It is particularly valuable for molecular identification, as each molecule possesses distinct chemical bonds and symmetry, which give rise to characteristic Raman spectral features. The technique is based on the principle of Raman scattering.



Fig. 2.7. Photograph of the LabRAM Raman spectroscopy system used for Raman characterization.

Credit:https://www.horiba.com/ind/scientific/products/detail/action/show/Product/labram-hr-evolution-1083/

When incident light falls on a material, the photons interact with the vibrational modes of its molecules, leading to the occurrence of both elastic and inelastic scattering of the light. These scattering processes involve an exchange of energy between the incident photons and the vibrational modes of atoms in the material. The basic working principle of Raman spectroscopy can be described as follows. A monochromatic laser beam is directed onto the sample surface, which results in the generation of both Rayleigh (elastic) and Raman (inelastic) scattered light from the illuminated region. The scattered light is then collected using an objective lens and passed through a monochromator that separates the light into different wavelengths. To remove the intense Rayleigh scattered light and selectively detect the Raman signal, a

notch filter is used. The filtered Raman signal is subsequently focused through a pinhole, which helps in improving the signal quality and minimizing background noise. The focused light is then directed into a spectrometer, where the spectral components are analyzed and optimized for better signal detection. Finally, the processed signal is detected using a charge-coupled device (CCD) detector. A digital image of the Raman spectroscopy instrument is shown in Fig. 2.7.

2.3.4. X-Ray Photoelectron Spectroscopy (XPS)

X-ray photoelectron spectroscopy (XPS) is a surface-sensitive spectroscopic technique used to determine the elemental composition as well as the chemical and electronic states of materials. Typically, XPS provides information from the top surface layer of a material, within a depth range of approximately 1-10 nm. The working principle of XPS is based on the photoelectric effect. When a solid sample is irradiated with monochromatic X-rays under ultra-high vacuum conditions, electrons-primarily core-level electrons-are emitted from the surface with characteristic kinetic energies. An XPS system mainly consists of a monochromatic X-ray source, an electron energy analyzer, and a high-vacuum chamber. The basic operational mechanism of XPS is illustrated in Fig. 2.8. The operation of the XPS technique involves several key steps. Initially, X-rays are produced when high-energy electrons strike a metal target. These X-rays are then monochromatized using optical components to obtain photons with a well-defined energy or wavelength. When the monochromatic X-rays irradiate the surface of the sample, core-level electrons are ejected from the atoms of the material. Only those electrons whose binding energy is lower than the energy of the incident photons can be emitted from the surface. The emitted photoelectrons are then directed toward a hemispherical energy analyzer, which consists of two concentric hemispherical electrodes-an outer electrode with a positive potential and an inner electrode with a negative potential. These electrodes are enclosed within magnetic shielding to ensure accurate electron trajectory control. The analyzer selectively allows electrons with

specific kinetic energies to pass through. Electrostatic lenses are used to guide the emitted electrons into the hemispherical analyzer while controlling their velocities through applied voltages. After passing through the analyzer, the electrons reach a detector that measures their number and kinetic energies.



Fig. 2.8. Photograph of the Thermo Scientific K-Alpha X-ray Photoelectron Spectrometer.

Credit:https://www.thermofisher.com/in/en/home/electron-microscopy/products/xps-instruments/instruments/k-alpha.html

Based on these measurements, a spectrum is generated that provides detailed information about the elemental composition and chemical states of the sample surface. In this thesis, XPS measurements of the synthesized samples were carried out using a Thermo Scientific K-Alpha X-ray photoelectron spectrometer.

2.3.5. Brunauer-Emmett-Teller (BET) Method

Brunauer-Emmett-Teller (BET) analysis is a widely used technique for determining the specific surface area of solid materials with high accuracy. This method is based on the physical adsorption of an inert gas onto the surface of the material. The amount of gas adsorbed on the surface depends

on several parameters, including the surface area of the material, temperature, gas pressure, and the manner in which the gas molecules engage with the solid surface.



Fig. 2.9. Camera image of BET Surface Area Analyzer

A fundamental parameter in BET analysis is the relative pressure (P/P_0), where P_0 represents the vapor pressure of the pure adsorbate at a given temperature and P denotes the partial pressure of the adsorbing gas. When the relative pressure (P/P_0) is below 0.01, physical adsorption is generally considered negligible. At approximately $P/P_0 \approx 0.1$, monolayer adsorption begins to form on the surface. As the adsorption process continues, the relative pressure gradually increases until it reaches $P/P_0 = 1$, which corresponds to saturation, beyond which no further adsorption occurs. For BET measurements, approximately 200–300 mg of powdered sample is typically required. Nitrogen (N_2) gas is commonly used as the adsorbate due to its inert nature, wide availability, and high purity. However, the interaction between nitrogen molecules and a solid surface is relatively weak at room or

elevated temperatures. Therefore, to enhance adsorption and ensure accurate measurements, the sample is generally cooled using liquid nitrogen, which significantly lowers the temperature of the system. During the BET analysis, nitrogen gas is gradually introduced into the sample chamber, and the change in pressure caused by gas adsorption is monitored using a highly sensitive pressure gauge. Once adsorption reaches equilibrium and no further gas uptake occurs, the sample is removed from the nitrogen atmosphere and subsequently heated to desorb the adsorbed nitrogen molecules. The collected adsorption-desorption data are then used to construct a BET isotherm, which represents the relationship between the amount of gas adsorbed and the relative pressure (P/P_0). Different types of adsorption isotherms provide insights into the pore structure and surface characteristics of the adsorbent material. Type I isotherms are typically associated with microporous materials, having pore diameters of ≤ 2 nm. Type II and Type III isotherms correspond to macroporous solids with pore diameters ≥ 50 nm; Type II indicates strong gas–solid interactions, whereas Type III reflects weaker interactions. Type IV isotherms are characteristic of mesoporous materials (pore diameters ≤ 50 nm) and usually exhibit a hysteresis loop due to capillary condensation within the pores. Type V isotherms are observed in porous materials where gas–solid interactions are relatively weak. In contrast, Type VI isotherms represent stepwise multilayer adsorption occurring on non-porous surfaces. These isotherm classifications provide valuable information regarding the surface properties, pore structure, and adsorption behaviour of solid materials. In this thesis, the BET surface area of the synthesized materials is determined using the Autosorb iQ2 system.

2.3.6. UV-Visible Spectroscopy

The interaction of light with matter results in several phenomena, including reflection, transmission, absorption, scattering, fluorescence, and phosphorescence. UV-Visible (UV-Vis) absorption spectroscopy is based on the absorption of light during its interaction with matter. When a sample is irradiated with light in the ultraviolet and visible regions of the

electromagnetic spectrum, the molecules absorb photons and undergo electronic transitions, which give rise to a characteristic UV-Vis absorption spectrum. Due to its reliability and simplicity, UV-Vis spectroscopy has become an important analytical technique for both qualitative and quantitative analysis of materials [7-8]. The absorption of ultraviolet and visible radiation by atoms or molecules is associated with the excitation of electrons from lower energy levels to higher energy states. Since the energy levels of atoms and molecules are quantized, only photons possessing a specific amount of energy can induce these electronic transitions. UV-Vis spectroscopy also provides information regarding the dispersion and homogeneity of a solution, which can be determined from the measured absorbance of the sample. The working principle of a UV-Vis spectrophotometer is based on the Beer-Lambert law. According to this law, when a beam of monochromatic light passes through a solution containing an absorbing species, the decrease in the intensity of the transmitted light is directly proportional to the concentration of the absorbing substance and the path length of the solution through which the light travels. The Beer-Lambert law can be expressed as:

$$A = \log\left(\frac{I_0}{I}\right) = \varepsilon lc \qquad (2.2)$$

where A represents the absorbance of the sample, I_0 is the intensity of the incident light, I is the intensity of the transmitted light, l denotes the path length of the sample, and ε is the molar absorptivity (or molar extinction coefficient), which indicates the probability of an electronic transition. According to this relationship, a higher number of molecules capable of absorbing light at a particular wavelength result in greater absorption of radiation. A UV-Vis spectrophotometer measures the absorbance of a sample over a range of wavelengths and records a spectrum in which absorbance (A) is plotted as a function of wavelength (λ) [9]. Experimental Setup of UV-Vis Spectrophotometer: The experimental setup of a UV-Vis spectrophotometer mainly consists of three essential components: a) Light source (UV and

visible region), b) Monochromator, c) Detector (such as a photomultiplier tube, photodiode, or charge-coupled device (CCD)). A schematic representation of the UV-Vis spectrophotometer is shown in Figure 2.4. To cover both the ultraviolet and visible spectral regions, two different light sources are generally used. A deuterium arc lamp (D_2 lamp) is employed for the ultraviolet region in the wavelength range of approximately 190-370 nm, whereas a tungsten lamp is used for the visible region covering approximately 320-1100 nm. The instrument automatically switches between these lamps while scanning across the UV and visible regions. The emitted light is dispersed into its component wavelengths using a prism or diffraction grating, allowing the intensity of light to be measured as a function of wavelength. Typically, the UV-Vis spectrophotometer operates as a double-beam instrument. In this configuration, the monochromatic light is directed through a system of mirrors that split the beam into two separate paths. One beam passes through the sample, while the other passes through a reference solution. The reference beam is considered to have 100% transmission (or zero absorbance), and the instrument measures the ratio of the transmitted intensities of the sample and reference beams. After passing through the sample and reference cells, the two beams are detected by a detector. The detector converts the received light into an electrical signal, and the output is recorded as a plot of intensity (or absorbance) versus wavelength, which provides valuable information about the optical properties of the sample. Commonly used detectors include photomultiplier tubes, photodiodes, and charge-coupled devices (CCD).

In the present study, the UV-Vis absorption spectra of pristine Co_3O_4, CTAB-assisted Co_3O_4 and CTAB-assisted 2.5 mol% Mo-doped Co_3O_4 were captured using a UV-Vis spectrophotometer (Shimadzu UV-2600i). A photographic image of the UV-Vis instrument used in this work is shown in Fig. 2.10.



Fig. 2.10. Digital image of UV-Vis Spectrometer

Credit:https://www.ssi.shimadzu.com/products/uv-vis/uv-vis-nir-spectroscopy/uv-2600i-plus-uv-2700i-plus/index.html

2.4. Dynamic Gas Sensing Setup

In this work, a dynamic flow-through gas sensing setup has been designed and implemented to analyze the performance of the fabricated sensors. Compared to conventional static measurement methods, the dynamic flow-through approach offers several advantages, particularly its capability to detect very low gas concentrations, even at the parts-per-billion (ppb) level. Additionally, this method provides greater flexibility for sensing measurements. Another important advantage is that the sensing chamber can be easily cleaned by passing synthetic air through it, eliminating the requirement for an expensive vacuum pump. The gas sensing measurements were carried out in a stainless-steel test chamber with an effective internal volume of approximately 500 cm^3. The chamber was equipped with a cylindrical heater interfaced with a proportional-integral-derivative (PID) temperature controller through electrical connections, allowing accurate control of the operating temperature throughout the sensing experiments. The contact pads of the sensor device (approximately 1 mm × 1 mm) are interfaced with a Keithley 2450 source meter. For resistance measurements, a

constant voltage of is applied using the Keithley 2450 sourcemeter, while the resistance exhibited by the sensing layer is continuously monitored and recorded on a computer. A mass flow controller (MFC; Alicat®, MC 1 slpm, USA) is employed to precisely regulate the gas flow rate within the system. High-purity gas cylinders (99.999% purity) of SO_2, CO, NO_2, NH_3, NO and CO_2 are used to create controlled gaseous environments at predetermined concentrations within the sensing chamber. To achieve lower gas concentrations, the target gas is diluted with synthetic air in a mixing chamber, where the flow rates of both gases are accurately regulated using mass flow controllers. To control the relative humidity (RH) inside the sensing chamber, a bubbler system is integrated into the air flow control line. The bubbler contains saturated aqueous solutions of different salts, such as K_2SO_4, NaCl, $NaNO_2$, $Mg(NO_3)_2 \cdot 6H_2O$, and $MgCl_2$, which generate approximate RH levels of 97.5%, 75%, 65%, 50% and 35%, respectively. This arrangement enables precise control of humidity conditions during sensing experiments. The sensor response can be expressed either as a ratio or in percentage form. The ratio-based response is expressed as R_{gas}/R_{air}, where R_{gas} represents the electrical resistance of the sensor when exposed to the target gas, and R_{air} denotes the baseline resistance of the sensor measured in ambient air. In percentage form, the sensor response is calculated using the following relation:

$$\text{Sensor Response (\%)} = \frac{R_{gas} - R_{air}}{R_{air}} \times 100 \qquad (2.4)$$

This expression represents the percentage variation in sensor resistance upon exposure to the target gas relative to its baseline resistance in ambient air.

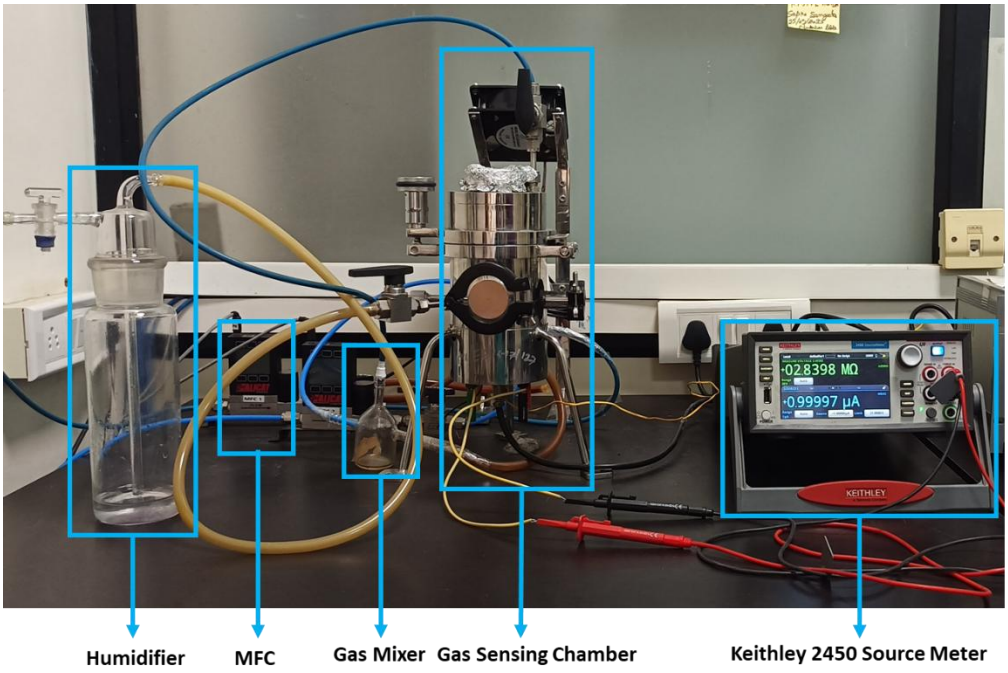


Fig. 2.11. Camera image of gas sensing setup.

2.5. References

[1] K. J. Hughes et al. "Nanoscience in action: Unveiling emerging trends in materials and applications." ACS omega, vol. 10, no. 8, pp. 7530-7548, 2025.

[2] A. K. Alves et al. “Hydrothermal Synthesis”, Novel Synthesis and Characterization of Nanostructured Materials, pp.61-76, 2013.

[3] Meskin, Pavel E., Vladimir K. Ivanov, Alexander E. Barantchikov, Bulat R. Churagulov, and Yury D. Tretyakov. "Ultrasonically assisted hydrothermal synthesis of nanocrystalline ZrO_2, TiO_2, $NiFe_2O_4$ and $Ni_{0.5}Zn_{0.5}Fe_2O_4$ powders." Ultrasonics sonochemistry, vol. 13, no. 1, pp. 47-53, 2006.

[4] Pan, Ding, Leonardo Spanu, Brandon Harrison, Dimitri A. Sverjensky, and Giulia Galli. "Dielectric properties of water under extreme conditions and transport of carbonates in the deep Earth." Proceedings of the National Academy of Sciences, vol. 110, no. 17, pp. 6646-6650, 2013.

[5] Ece, Özlem. (2012) Hydrothermal synthesis and structural characterization of open-framework metal phosphates templated with organic diamines. MSc. Dissertation, Izmir Institute of Technology (Turkey).

[6] M. Lee, “X-Ray diffraction for materials research: from fundamentals to applications,” CRC Press, 2017.

[7] Rizwan, Mohammad, and Christopher Gwenin. "Nanomaterials in renewable energy: UV-Visible spectroscopy characterization and applications." In Nano tools and devices for enhanced renewable energy, Elsevier, pp. 103-120, 2021.

[8] Dubey, Rajni, Ashish Kumar, and Bhaskar Kumar Gupta. "A review of UV-Visible spectroscopy: techniques and applications." International Journal of Novel Research and Development, vol. 9, no. 10, pp. b412-b423, 2024.

[9] Alaboodi, Azhar S., Shaymaa Awad Kadhim, and Ahmed Shaker Hussein. "Ultraviolet-Visible Spectroscopy, Importance, Principle, Structure and Most Important Applications: A Study Review." Int. J. Nov. Res. Phys. Chem. Math, vol.12, pp. 53-60, 2025.

Chapter 3

Room-Temperature CO Detection Using CTAB-Assisted Mo-Doped Co_3O_4 Nanoflowers

3.1. Introduction

Carbon monoxide (CO) is a highly toxic, colourless, and odourless gas primarily generated from the incomplete combustion of carbon-containing materials such as wood, charcoal, and gasoline, as well as from natural and anthropogenic sources including wildfires, vehicular emissions, and biomass burning [1]. Inhalation of CO poses severe health risks, as it readily binds with haemoglobin to form carboxyhaemoglobin, thereby significantly reducing the oxygen-carrying capacity of blood and inducing hypoxia in vital organs [2]. Depending on the level and duration of exposure, the resulting health effects may range from mild symptoms such as dizziness, nausea, headache, and blurred vision to severe conditions including seizures, cardiac arrest, and even death [2]. The permissible exposure limit of CO according to US Occupational Safety and Health Administration (OSHA) is 50 ppm for 8-hour time - weighted average [3]. Thus, a highly efficient low-cost CO gas sensor is to be fabricated for room temperature detection of CO.

Metal oxide semiconductor (MOS)-based gas sensors have demonstrated excellent capability for detecting a wide range of hazardous gases, including CO, NO_2, and NH_3, and have remained a subject of extensive research since the first MOS-based gas sensor was patented by Naoyoshi Taguchi in 1962 [4-6]. Additionally, MOS materials offer several advantages, including compatibility with simple and cost-effective fabrication techniques, along with desirable device characteristics such as ease of operation, high stability, and rapid response and recovery times [7-8].

Among the MOSs explored for gas sensing applications, cobalt oxide (Co_3O_4) has gained considerable interest owing to its favourable physicochemical properties. It has a spinel structure with Co^{2+} at the tetrahedral site and Co^{3+} at the octahedral site, demonstrating variable oxidation states. Co_3O_4 shows a

redox nature and hence sensitive towards CO [9]. It has been widely used to detect various kinds of toxic gases due to its good catalytic activity [10-11]. Despite significant advancements in CO sensing technologies, many MOS-based sensors still suffer from limitations such as high operating temperatures, sluggish response-recovery characteristics, and poor selectivity [12]. While Co_3O_4 is widely studied for its catalytic activity and stability, improving its sensitivity and response kinetics remains crucial for practical use. Strategies such as transition metal modification and surfactant-assisted morphology control have demonstrated enhanced gas-sensing performance; however, their combined effects in Co_3O_4-based systems remain relatively underexplored [13].

For the synthesis of these transition metal oxides (TMOs) various techniques have been undertaken such as sol gel, thermal decomposition, hydrothermal synthesis, electrodeposition and chemical vapour deposition [14]. S.Farhadi et al. reported synthesis of Co3O4 nanoparticles via thermal decomposition to investigate optical and magnetic properties of Co_3O_4 [15]. A.W. Alrowaily et al. reported Nd-doped Co_3O_4 nanostructures via hydrothermal technique as electrodes for supercapacitor application [16]. C. Lohaus et al. synthesized Co_3O_4 thin films for solar energy conversion via RF Magnetron Sputtering [17]. While each method offers its unique ability to tailor the morphology, topology, and electronic characteristics of the synthesized material, hydrothermal synthesis is widely regarded as a facile and cost-effective approach due to its simplicity, scalability, and economic viability, while also enabling the production of metastable materials with high crystallinity and purity [18]. The sensing properties of Co_3O_4 can be enhanced by modifying its morphology, doping with other elements, decorating it with noble metals, and forming heterojunctions [19]. Tao et al. reported that Fe-doped Co_3O_4 demonstrated a response of 34.5 for 100 ppm of xylene [20]. Qu et al. reported Ni-doped SnO_2 with a response of 7.28 for 50 μL/L of CO [21]. Bekermann et al. reported Co_3O_4/ZnO nanocomposite synthesized via Plasma Enhanced Chemical Vapour Deposition for Gas Sensing [22].

In this work, a Cetyltrimethylammonium Bromide-assisted Mo-doped Co_3O_4 (CTAB-assisted Mo-doped Co_3O_4) gas sensor for CO sensing has been fabricated via a facile hydrothermal method. CTAB serves as a structure-directing surfactant, while Mo incorporation modifies the electronic properties of Co_3O_4; collectively, these effects synergistically enhance the gas-sensing response. Three types of samples were investigated: pristine Co_3O_4, CTAB-assisted Co_3O_4 and CTAB-assisted Mo-doped Co_3O_4. Further voltage bias variation has been carried out to investigate the optimized sensitivity of the sensor. Among all the performed experiments CTAB-assisted 2.5 mol% Mo-doped Co_3O_4 at an applied bias voltage of 5V shows the highest sensitivity of 4188% with an exceptional response and recovery time of 42 s and 54 s respectively, at 100 ppm of CO at room temperature (25ºC).

3.2. Experimental

3.2.1. Materials

Ammonium molybdate tetrahydrate ($(NH_4)_6Mo_7O_{24}.4H_2O$) and CTAB were both purchased from Sigma-Aldrich Chemical Pvt. Ltd. Ammonium solution (NH_4OH, 25%) was purchased from Expresolv Pvt. Ltd. and Cobalt (II) nitrate hexahydrate (Co $(NO_3)_2 \cdot 6H_2O$) was purchased from Siscon Research Laboratories Pvt. Ltd., India. The chemicals utilized in this study were of analytical grade and procured from commercial suppliers; they were used as received without any further purification.

3.2.2. Synthesis Process

Pristine-Co_3O_4, CTAB-assisted Co_3O_4 (C- Co_3O_4) and CTAB assisted Mo-doped Co_3O_4 (C-Mo-Co_3O_4) were synthesized via the hydrothermal method. Pristine-Co_3O_4 solution was synthesized by dissolving 0.1 M of $(Co(NO_3)_2 \cdot 6H_2O$ in 50 mL of deionized (DI) water under constant magnetic stirring for 30 minutes. Ammonia solution (approx. 30 mL) was then added dropwise until the pH reached 11. The resulting solution was transferred to a 100 mL Teflon-lined stainless-steel autoclave and heated at 120 ℃ for 6 h in

a hot air oven. After being naturally cooled to room temperature, the precipitate was collected, washed thoroughly with DI water and ethanol repeatedly, dried at 80 °C for 14 h, and finally annealed at 500 °C for 3 h to obtain pure Co_3O_4.

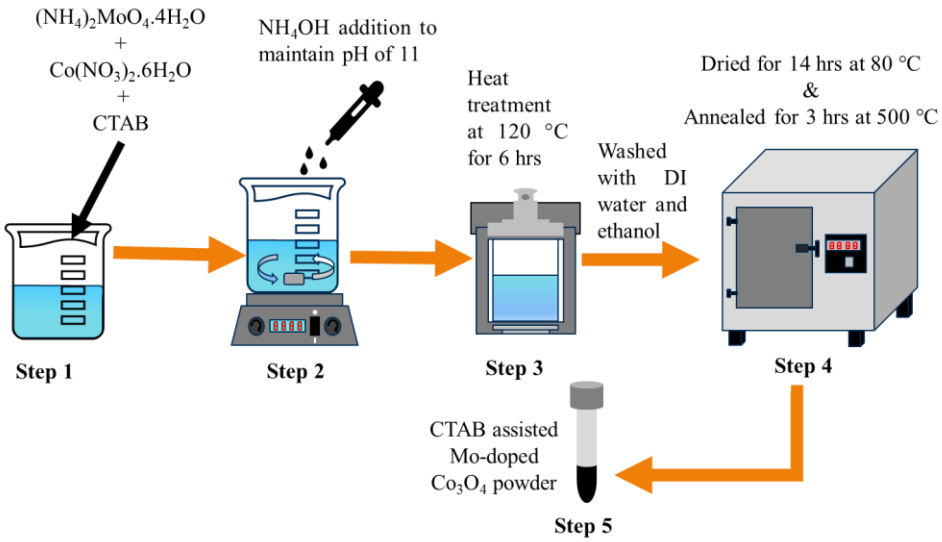


Fig. 3.1. Schematic diagram for synthesis of CTAB assisted Mo doped Co_3O_4

For C- Co_3O_4 synthesis, the same procedure was opted with the addition of 0.025 M CTAB to the precursor solution. Similarly, C-1.5% Mo-Co_3O_4, C-2.5% Mo-Co_3O_4, C-3.5% Mo-Co_3O_4 samples were synthesized by incorporating 1.5 mol%, 2.5 mol%, and 3.5 mol% of $(NH_4)_6Mo_7O_{24}.4H_2O$ along with 0.025 M CTAB into the reaction mixture respectively. The resulting powders were dispersed in DI water. This mixture was drop-cast onto the interdigitated electrodes (IDEs) using a 10 µL micropipette for sensor fabrication. The synthesis process has been schematically shown in Fig. 3.1.

3.2.3. Characterization

Various characterization techniques were undertaken to investigate the crystallinity, phase, morphology, surface area and bandgap of the synthesized samples. The crystal structure and phase of the synthesized sample are analysed by X-ray Diffraction (XRD) pattern obtained using Rigaku Smart Laboratory Automated X-ray diffractometer operated at 30 kV, 15 mA with

Cu-Kα, X-ray (λ = 1.54 Å) with a scan rate of 2°/min. The morphological structure is studied via the Zeiss Gemini SEM 360 field emission scanning electron microscope (FESEM) instrument. The specific surface area was determined using the Autosorb iQ2 instrument, employing the Brunauer-Emmett-Teller (BET) method with nitrogen (N_2) adsorption-desorption isotherms. The bandgap and elemental composition were determined using Shimadzu UV-2600i instrument and X-ray Photoelectron Spectroscopy (XPS, ULVAC PHI Quantra II, Al Kα radiation, 1486.6eV) respectively.

3.2.4. Device fabrication and gas sensing measurements

The synthesized sensing material was deposited onto IDEs comprising 20/200 nm, Ti/Pt layers, with an electrode width of 50 µm and an inter-electrode spacing of 25 µm, via a drop casting technique. Each electrode was connected to a $1 \times 1\ mm^2$ contact pad for electrical interfacing (Fig. 3.2). Titanium was selected as an adhesion layer, providing strong bonding between the platinum film and the quartz surface, while platinum was chosen as the primary contact metal due to its excellent electrical conductivity, chemical inertness, thermal stability, and compatibility with high-temperature gas-sensing operations [23-24]. The use of quartz as the substrate further ensures minimal parasitic conduction, thermal durability, and mechanical stability, making it an ideal platform for resistive gas sensing [23-24]. Gas sensing measurements were carried out in a dynamic flow stainless-steel chamber with a total volume of 500 cm^3. The electrical response of the sensor was recorded using a Keithley 2450 Source Meter, which supplied a constant bias voltage of +5 V and simultaneously measured the dynamic resistance of the sensing layer. The target gas concentrations were regulated using mass flow controllers (MFCs), and the gas flow rate was maintained at 500 sccm. High-purity gas cylinders (99.999%) containing SO_2, CO, NO_2, NH_3, NO and CO_2 were used to generate controlled test atmospheres within the chamber. Response of the sensor is calculated by, Response = $|(R_g - R_a)/R_a|$ x 100%, where, R_g and R_a denote the sensor resistance under target gas and ambient

air exposure, respectively. The schematic illustration of the entire gas sensing setup has been shown in Fig. 3.3.

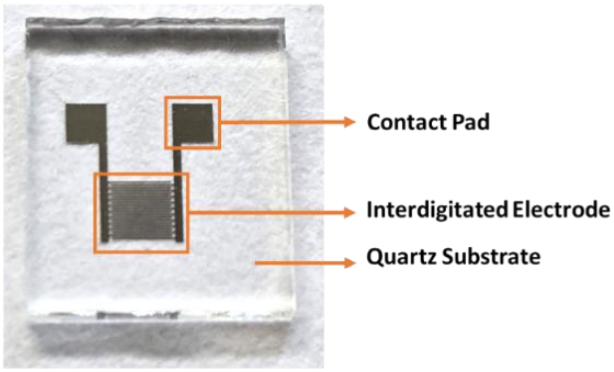


Fig. 3.2. Camera image of IDEs.

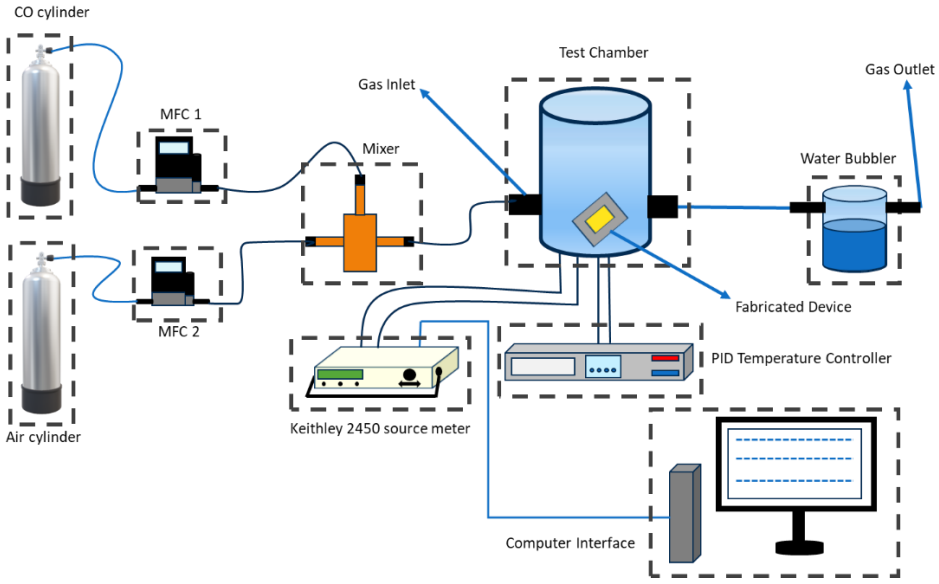


Fig. 3.3. Schematic diagram of gas sensing setup used in this work

3.3. Results and Discussion

3.3.1. Surface Morphological Analysis

3.3.1.1. Field Emission Scanning Electron Microscopy Analysis

Surface morphologies of pristine-Co_3O_4, C-Co_3O_4 and C-Mo-Co_3O_4 have been shown in Fig. 3.4. Pristine-Co_3O_4 exhibits a nanosphere-like morphology whereas a distinct change in morphology from nanosphere to

nanoflowers is observed in C-Co_3O_4 and C-Mo-Co_3O_4 as shown in Fig. 3.4 (b)-(d). No significant change in the surface morphology of C-Mo-Co_3O_4 is observed with varying Mo doping concentrations, likely due to the low dopant content. In contrast, the pronounced variation in surface morphology underscores the critical role of the surfactant (CTAB) during the hydrothermal synthesis of Mo-doped Co_3O_4.

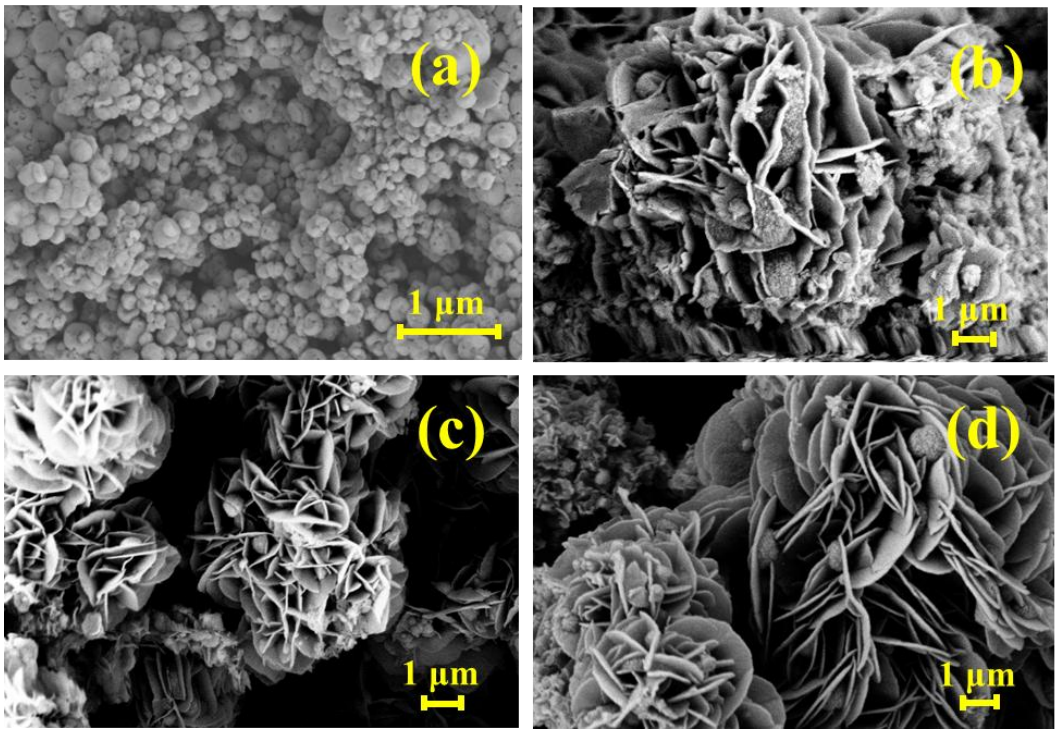


Fig. 3.4. FESEM images of (a) Pristine-Co_3O_4, (b) C-Co_3O_4, (c) C-Mo-Co_3O_4, (d) Magnified image of C-Mo-Co_3O_4.

3.3.1.2. XRD and BET Analysis

The crystallographic structure and phase of pristine-Co_3O_4, C- Co_3O_4, C-1.5% Mo-Co_3O_4, C-2.5% Mo-Co_3O_4 and C-3.5% Mo -Co_3O_4 were investigated via X-ray Diffraction (XRD) as shown in Fig. 3.5(a). The XRD spectra correspond to various planes such as (111), (220), (311), (400) (422) and, (511). As depicted in Fig. 3.5(a), the diffraction peaks of pristine sample correspond closely to cubic spinel Co_3O_4 (JCPDS card No. 42 1467) [25]. The absence of Mo-related diffraction peaks in the C-Mo-Co_3O_4 indicate very

low content of Mo. A slight shift in the (311) and (220) peaks confirm successful Mo^{6+} doping into the Co_3O_4 lattice. Furthermore, the absence of secondary or impurity peaks, along with the presence of sharp and well-defined diffraction peaks in the XRD pattern, indicates the high phase purity and good crystallinity of the synthesized C Mo-Co_3O_4.

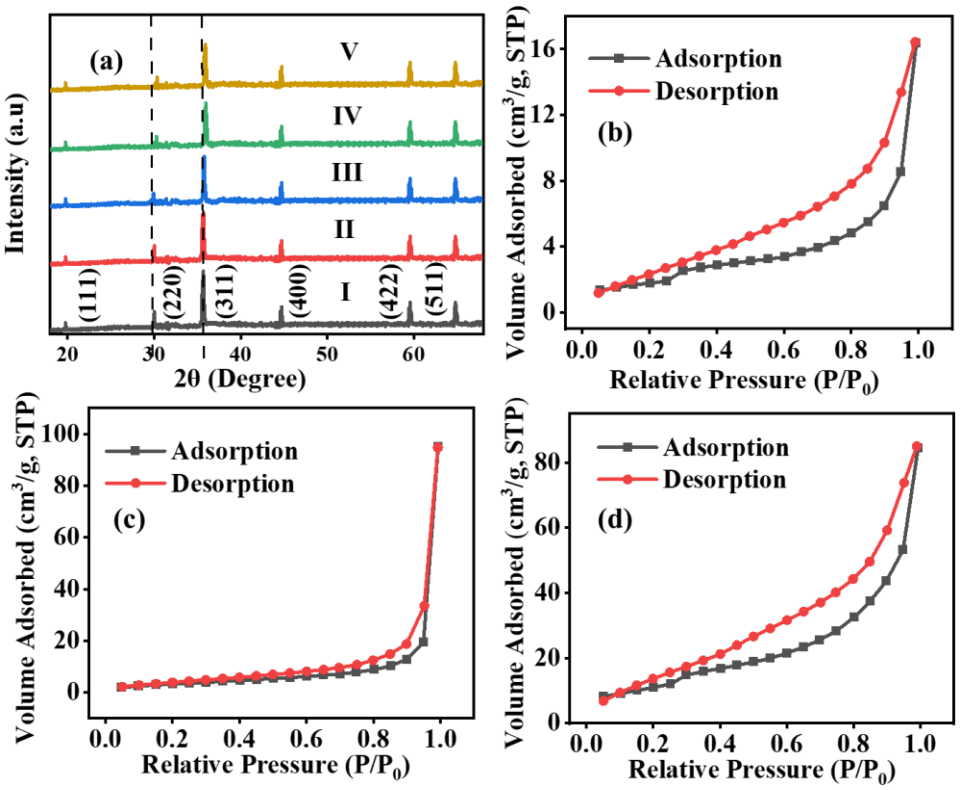


Fig. 3.5. (a) XRD spectrum of pristine-Co_3O_4 (I), C-Co_3O_4 (II), C-1.5% Mo-Co_3O_4 (III), C-2.5% Mo-Co_3O_4 (IV), C-3.5% Mo-Co_3O_4 (V); Nitrogen adsorption-desorption profile for (b) pristine- Co_3O_4, (c) C Co_3O_4, (d) C-2.5% Mo-Co_3O_4.

Fig. 3.5 (b-d) shows the nitrogen adsorption- desorption isotherms of pristine-Co_3O_4, C-Co_3O_4, and C-2.5% Mo-Co_3O_4, displaying a type - IV isotherm with an H3 hysteresis loop, confirming their mesoporous nature [26]. The BET derived specific surface area of the pristine-Co_3O_4 nanospheres is found to be 7.467 m^2/g, while the C-Co_3O_4 nanoflowers exhibit an increased surface

area of 12.864 m^2/g. Notably, the surface area further increases to 46.519 m^2/g upon Mo doping in C-Co_3O_4 nanoflowers.

3.3.1.3. XPS Analysis

X-ray photoelectron spectroscopy (XPS) was used to investigate the elemental composition and chemical states of the synthesized materials. The analysis was performed on a ULVAC-PHI Quantra II system incorporating an Al Kα (1486.6 eV) X-ray source. The survey spectra (Fig. 3.6 (a-b)) confirm the presence of Cobalt (Co), Oxygen (O), and Molybdenum (Mo). The high-resolution Co 2p spectrum (Fig. 3.6(c)) exhibits two main spin-orbit doublets. The peaks centred at approximately 780.38 eV and 796.08 eV are assigned to Co $2p_{3/2}$ and Co $2p_{1/2}$, respectively. An energy separation of approximately 15.7 eV was observed between the two peaks, corresponding to spin-orbit splitting and confirming the presence of both Co^{2+} and Co^{3+} oxidation states [27]. Deconvolution of the Co $2p_{3/2}$ peak reveals components at 779.2 eV and 781.2 eV, corresponding to Co^{3+} and Co^{2+} oxidation states, respectively, which are characteristic of Co_3O_4. Similarly, the Co $2p_{1/2}$ peak was fitted with two components at 795.2 eV (Co^{3+}) and 797.2 eV (Co^{2+}). Additionally, two shake-up satellite peaks were observed at 789.38 eV and 804.88 eV, consistent with previously reported data for Co_3O_4 [28]. The Mo 3d spectrum (Fig. 3.6 (d)) displays a doublet with peaks at binding energies of 231.98 eV (Mo $3d_{5/2}$ and 235.08 eV (Mo $3d_{3/2}$). The spin-orbit splitting of 3.19 eV confirms the presence of Mo^{6+} in the Mo-doped Co_3O_4 lattice [29-30]. The O 1s spectra for both pristine Co_3O_4 and the CTAB-assisted Mo-doped Co_3O_4 (Fig. 3.6 (e-f)) were deconvoluted into three constituent peaks, representing lattice oxygen (O_L) at 529.65 eV, oxygen vacancies (O_V) at 531.26 eV, and chemisorbed oxygen species (O_C) at 533.48 eV [31-32]. Quantitative analysis revealed a significant increase in the proportion of oxygen vacancies (O_V) in the CTAB-assisted Mo-doped Co_3O_4 (41.8%) compared to the pristine Co_3O_4 (24%).

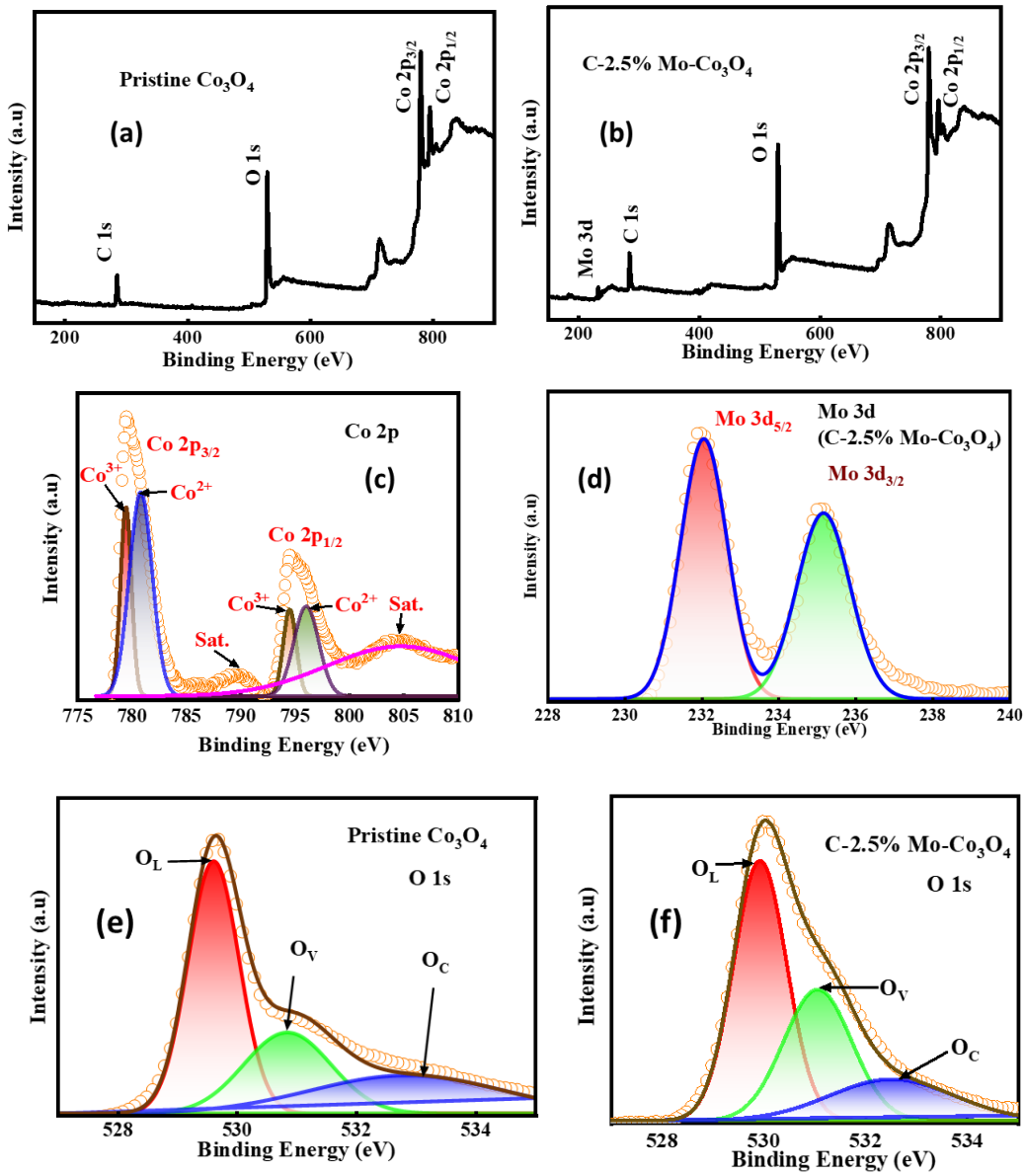


Fig. 3.6. (a) XPS survey spectra of pristine Co_3O_4, (b) XPS survey spectra of CTAB assisted Mo doped Co_3O_4, (c) Co 2p, (d) Mo 3d, (e) O 1s spectra for pristine Co_3O_4, (f) O 1s spectra for CTAB assisted Mo-doped Co_3O_4

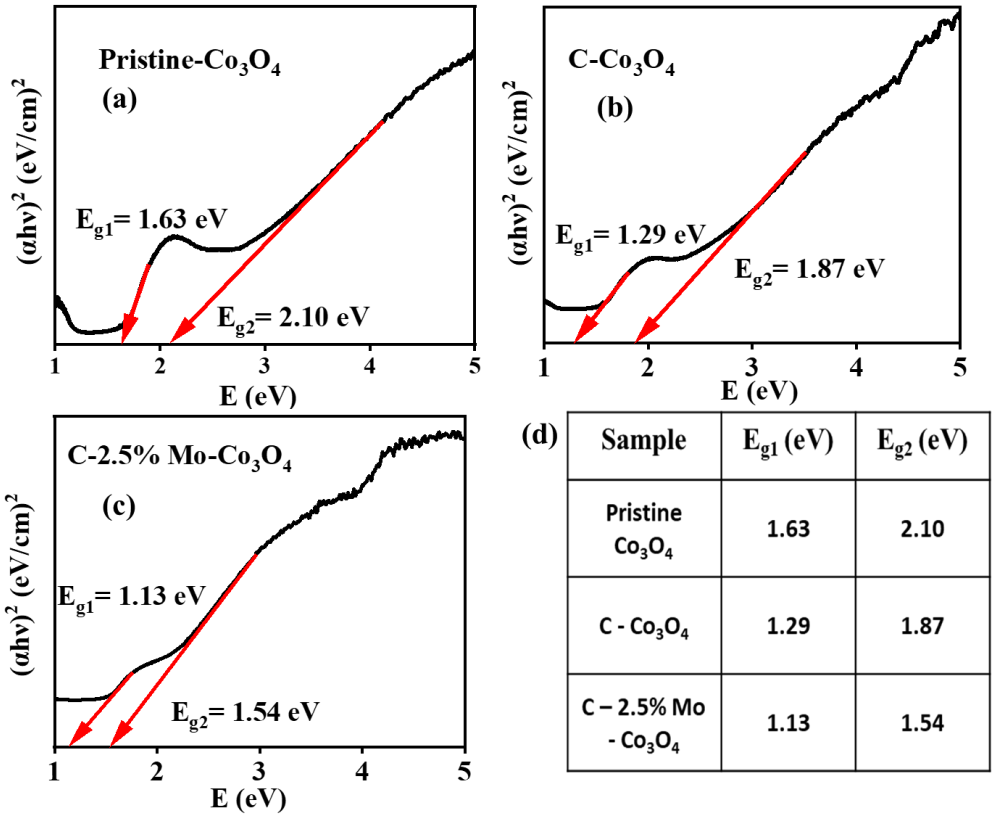
This enhancement in oxygen vacancy concentration provides more active sites for surface reactions, thereby improving the gas sensing response of the material. Consequently, the superior sensing performance arises from the higher density of oxygen vacancies in the CTAB-assisted Mo-doped Co_3O_4.

3.3.1.4. UV-Vis Analysis

The bandgap of pristine-Co_3O_4, C-Co_3O_4 and C-2.5% Mo- Co_3O_4 were investigated via UV-Vis Spectroscopy using the Tauc relation:

$$(\alpha h\nu)^n = A(h\nu - Eg) \quad (3.1)$$

where α is the absorption coefficient, h is the Planck's constant, ν is frequency of light, Eg is the bandgap energy, A is the constant characteristic, n equals to 1/2 for indirect transition and 2 for a direct transition. The bandgap values of the materials were determined from $(\alpha h\nu)^2$ vs. hν plots as shown in Fig. 3.7(a-c) by extrapolating to α = 0.



(d)

Sample	E_{g1} (eV)	E_{g2} (eV)
Pristine Co_3O_4	1.63	2.10
C - Co_3O_4	1.29	1.87
C – 2.5% Mo - Co_3O_4	1.13	1.54

Fig. 3.7. Bandgap energy of (a) pristine-Co_3O_4, (b) C-Co_3O_4, (c) C 2.5%-Mo-Co_3O_4 and (d) Tabular representation of bandgap energy of pristine -Co_3O_4, C-Co_3O_4, C-2.5%-Mo-Co_3O_4.

The Tauc plots reveal two optical transitions: the lower bandgap (E_{g1}) corresponds to $O_{2p} \rightarrow Co^{3+}$ excitation, while the higher bandgap (E_{g2}) arises from $O^{2-} \rightarrow Co^{2+}$ charge transfer. In the Co_3O_4 spinel structure, Co^{3+} introduces sub-bands within the energy gap. Hence, E_{g2} represents the actual band gap as it corresponds to inter-band transition [33-34]. Fig. 3.7 (d) shows a progressive bandgap reduction from pristine-Co_3O_4 to C-2.5% Mo-Co_3O_4, attributable to CTAB modification and Mo doping-induced defects, oxygen vacancies, and intermediate states [35-36]. This bandgap narrowing promotes low-energy charge transfer, enabling efficient electron-hole generation without thermal activation, thereby enhancing RT CO sensing performance.

3.3.2. Sensing Performance Analysis

The gas sensing response of pristine-Co_3O_4, C-Co_3O_4, C-1.5% Mo-Co_3O_4, C-2.5% Mo-Co_3O_4 and C-3.5% Mo-Co_3O_4 toward 100 ppm CO at RT is shown in Fig. 3.8 (a). The pristine Co_3O_4 exhibits a response of 63%, whereas CTAB modification significantly enhances the response to 278.5%, attributed to the increased surface area (from 7.467 m^2/g to 12.864 m^2/g) and morphological transformation from nanospheres to nanoflowers. Furthermore, Mo-doped Co_3O_4 sensors demonstrate enhanced sensing responses of 2067%, 4188%, and 1670%, compared to the response of 278.5% observed for the C-Co_3O_4 sensor.

This improvement is attributed to the incorporation of Mo adatoms, which introduce additional active sites on the Co_3O_4 surface and thereby enhancing the sensing performance. Notably, Mo doping at 1.5 mol% and 2.5 mol% significantly increases the sensing response from 2067% to 4188%, as illustrated in Fig. 3.8 (a). Due to the remarkable sensing capability of C-2.5 % Mo Co_3O_4 we have considered it for further sensing performance investigation. Selectivity studies, as shown in Fig. 3.8 (b), are conducted using NH_3 (500 ppm), NO_2, CO_2, NO, and SO_2 (each at 100 ppm), revealing a marked preference for CO, thus highlighting the ultrasensitive nature of the sensor. The high selectivity toward CO can be attributed to the presence of

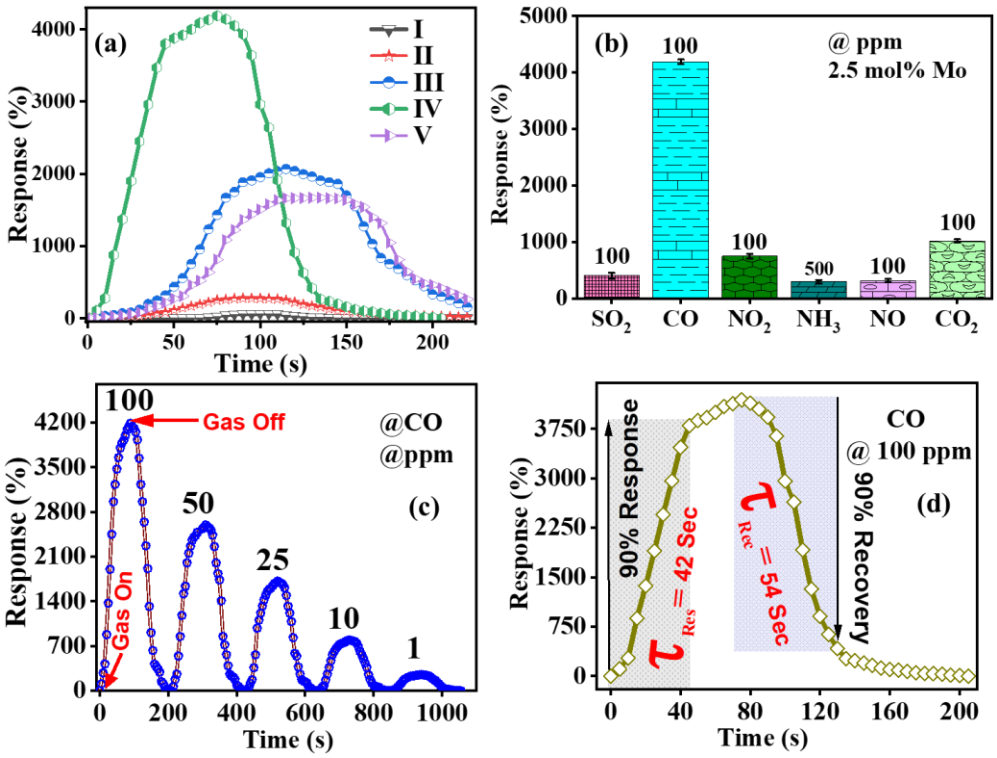


Fig. 3.8: (a) Sensing performance of pristine-Co_3O_4 (I), C-Co_3O_4 (II), C-1.5% Mo-Co_3O_4 (III), C-2.5% Mo-Co_3O_4 (IV), C-3.5% Mo-Co_3O_4 (V); (b) Selectivity analysis of C-2.5% Mo-Co_3O_4, (c) Response of C 2.5% Mo-Co_3O_4 at varying CO concentrations (d) Transient analysis of C-2.5% Mo-Co_3O_4.

abundant Co^{3+} catalytic sites and the increased oxygen vacancy concentration induced by Mo doping, as confirmed by XPS analysis. The higher density of oxygen vacancies promotes the adsorption of reactive oxygen species, which readily participate in oxidation reactions with CO molecules. This synergistic effect facilitates CO activation at room temperature, resulting in preferential interaction compared to other interfering gases [37-39]. The gas sensing performance of the C-2.5% Mo-Co_3O_4 sensor is investigated at RT over a range of CO concentrations from 100 ppm to 1 ppm, as illustrated in Fig. 3.8 (c). The sensor response exhibits a gradual decline from 4188% to 244.45% with decreasing CO concentration. Notably, even at a low concentration of 1 ppm, the C-2.5% Mo-Co_3O_4 sensor maintains a high response of 244.45%, indicating excellent sensitivity. The sensor also shows rapid response (42 s)

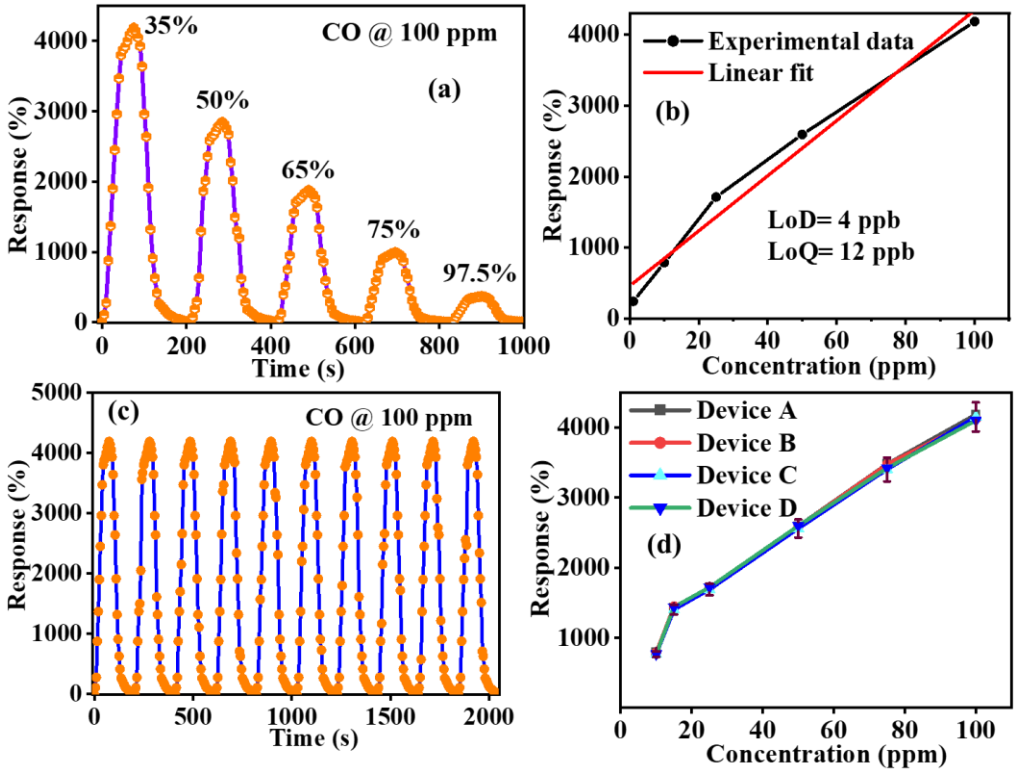


Fig. 3.9: Operational analysis of C-2.5% Mo-Co_3O_4 (a) Relative humidity (RH) analysis (b) LoD and LoQ (c) Repeatability analysis for 10 cycles (d) Reproducibility with error bars.

and recovery (54 s) times at 100 ppm CO and RT (Fig. 3.8 (d)), indicating its strong potential for real-time gas monitoring applications. The sensing performance of C-2.5% Mo-Co_3O_4 was investigated under varying humidity (35% - 97.5% RH) at RT in the presence of 100 ppm CO. As shown in Fig. 3.9(a), even at 97.5% the sensor shows a response of 376.92%, attributed to water molecule adsorption reducing the active surface area. The limit of detection (LoD) and limit of quantification (LoQ) are two additional critical parameters for evaluating the sensitivity and analytical performance of the sensor. The LoD and LoQ are defined by the following equations:

$$LoD = 3N_{rms}/\ Slope \tag{3.2}$$

$$LoQ = 3LoD \tag{3.3}$$

where N_{rms} represents the baseline standard deviation of the sensor resistance in ambient air, while the slope is calculated from the linear fit of the sensor response as a function of gas concentration, as shown in Fig.3.9(b). The fabricated sensor demonstrates a LoD of 4 ppb and LoQ of 12 ppb as shown in Fig. 3.9(b). The LoQ is typically defined as nearly three times the LoD, ensuring compliance with the performance standards required for commercial and industrial sensor applications [40]. Repeatability tests over 10 cycles (Fig. 3.9c) reveal excellent stability, with consistent responses upon repeated CO exposure, confirming reliable performance. To investigate reproducibility, four devices were fabricated using the same method described above, and all of them exhibited consistent results across different CO concentrations, as shown in Fig. 3.9 (d).

The long-term stability of the sensor was assessed over two months under ambient conditions (Fig. 3.10 a), showing no sensitivity degradation. This consistent performance confirms its suitability for prolonged use. Fig. 3.10 (b) shows the current - voltage (I-V) characteristics of pristine-Co_3O_4, C-Co_3O_4, and C-Mo-Co_3O_4 under 0 to 5 V DC bias. The I-V curves exhibit nonlinear behaviour, indicating the rectifying nature of the Co_3O_4 - based sensors. A noticeable enhancement in current is observed upon CTAB modification and Mo doping. Specifically, the current increases progressively from pristine Co_3O_4 to C-Co_3O_4, and further with increasing Mo doping concentrations (1.5%, 2.5%, and 3.5%). This suggests that Mo doping enhances the electrical conductivity of the Co_3O_4 nanostructures, likely due to increased carrier concentration and improved charge transport, which are beneficial for sensing applications.

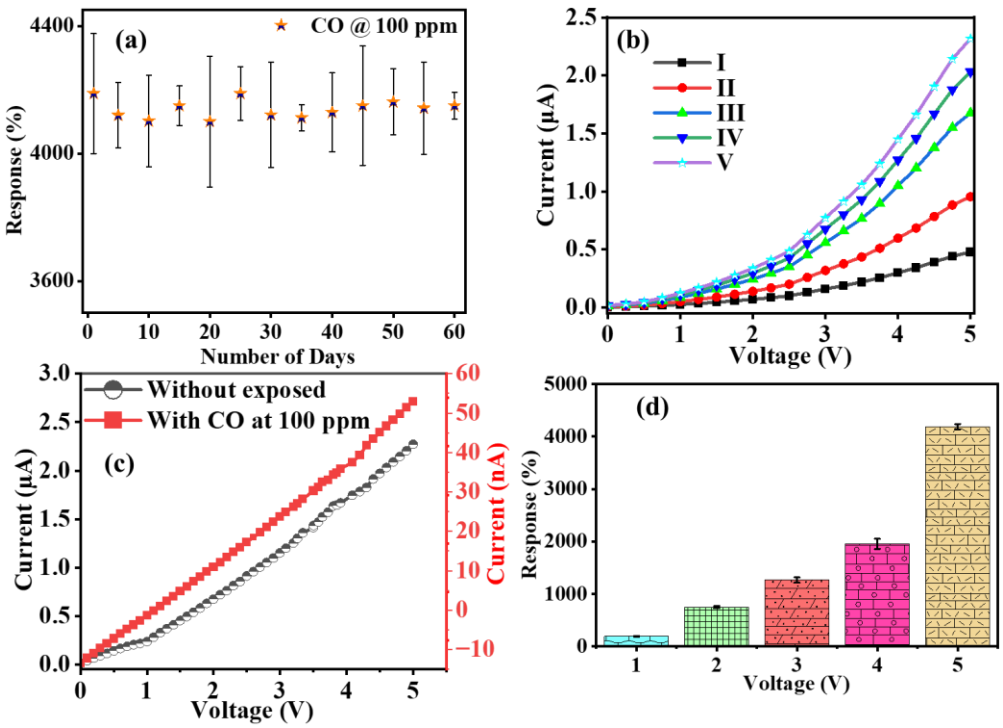


Fig. 3.10. (a) Long term stability analysis of C-2.5% Mo-Co_3O_4, (b) I-V characteristics of pristine-Co_3O_4 (I), C-Co_3O_4 (II), C- 1.5% Mo-Co_3O_4 (III), C-2.5% Mo-Co_3O_4 (IV), C-3.5% Mo-Co_3O_4 (V); (c) I-V plot of C-2.5%-Mo-Co_3O_4 with and without exposure to CO and (d) Change in response with bias voltage for C-2.5%-Mo- Co_3O_4

As depicted in Fig 3.10 (d), the response of the sensor to CO is strongly reliant on the applied bias voltage. At higher bias voltages, the separation and transport of charge carriers are enhanced, which amplifies the current difference between the unexposed and exposed conditions. Thus, the applied bias voltage plays a significant influence. Table I compares the CO-sensing performance of C-2.5% Mo -Co_3O_4 with other reported sensors. Our material demonstrates superior room-temperature response, resulting from synergistic effects of CTAB templating and Mo doping in the Co_3O_4 lattice. Mo doping introduces additional oxygen vacancies that effectively trap CO molecules, significantly enhancing sensitivity. The dopant provides a catalytic effect while lowering the activation energy for oxygen ions and the gas interactions, enabling efficient electron transfer. C.N. Wang et al. [41] reported doping

with metal elements such as Mo increases carrier concentration by releasing additional free electrons, while also creating structural defects and oxygen vacancies that enhance gas-solid interactions. C. Shen et al. [42] reported that 4% Mo doping in $LaFeO_3$ nearly doubled the BET surface area (from 5.7 to 10.5 m^2/g) and enhanced the sensor response by 11 times toward triethylamine. Literature confirms that optimized Mo doping improves both response and reduces operating temperature [43]. CTAB serves as both a surface modifier and a surface activity-enhancing agent, promoting the formation of additional active sites for oxygen adsorption and thereby improving the gas-sensing performance. This facilitates faster adsorption-desorption kinetics, enabling efficient oxygen molecule trapping and enhanced response. Additionally, CTAB controls particle size and morphology, yielding smaller grains with higher surface-to-volume ratios that further boost sensing performance [44-45]. R.K. Bedi et al. [46] reported an approximately 12-fold increase in the ammonia sensing response at room temperature for CTAB-assisted CuO nanostructures compared to those synthesized without any surfactant. This enhancement was attributed to the increased porosity resulting from structure-directing properties of CTAB. Similarly, D. Meng et al. [47] observed that the specific surface area of WO_3 synthesized with CTAB increased significantly from 4.5 to 28.3 m^2/g, leading to markedly higher H_2 sensitivity at all tested concentrations.

The extraordinary sensitivity of C-2.5% Mo-Co_3O_4 sensor depicts its proficiency for detecting CO at room temperature. This sensor shows a high sensitivity, rapid response and recovery time, good long-term stability and remarkable repeatability. These prominent features indicate its prospective application in real-time monitoring of environmental toxic gas pollution.

Table 3.1: Comparative analysis with published literature

S. N.	Sensing Material	Conc.[a] (ppm)	T[b] (°C)	R[c] (%)	τ_{res}/τ_{rec} (s)	Ref.
1.	CuO/rGO	1	RT[d]	2.56	70/160	[48]
2.	SnO_2 doped MoO_3 nanofibers	300	350	41.6	1430/1524	[49]
3.	$SnSe_2$ loaded ZnO	200	RT	14.8	19/13	[50]
4.	MOF-derived SnO_2/NiO	100	30	5.48	56/4	[51]
5.	SnO_2/$MoSe_2$	100	RT	9.2	20/16	[52]
6.	Pd-WSe_2	5	RT	9.25	52/97	[53]
7.	2D-CuO nanosheets	100	RT	3860	100/72.4	[54]
8.	CuO nanoplatelets	20	RT	1510	81/76	[55]
9.	rGO-α-Fe_2O_3 nanocomposite	50	RT	700	21/8	[56]
10.	**C–2.5% Mo-Co_3O_4**	**100**	**RT**	**4188**	**42/54**	**Our work**

[a]Concentration, [b]Temperature, [c]Response, [d]Room temperature

3.3.3. Sensing Mechanism

The sensing mechanism of the developed sensor is predominantly influenced by the adsorption and desorption dynamics of oxygen species on the surface of the material, which are strongly dependent on the operating temperature. At relatively low temperatures (below 100 °C), molecular oxygen ions (O_2^-) are the dominant adsorbed species. In the intermediate temperature range (100-300 °C), atomic oxygen ions (O^-) are the most stable, while at higher temperatures (above 300 °C), divalent oxygen ions (O^{2-}) prevail [57]. These oxygen species act as reactive centres for analyte-gas interactions, playing a decisive role in modulating the sensing response. When the sensor is exposed to ambient air, oxygen molecules from the atmosphere adsorb onto the surface of the sensing material and capture electrons from the conduction band of the oxide semiconductor, leading to generation of negatively charged oxygen species (mainly O_2^- under the present conditions). This electron withdrawal process creates a hole accumulation layer near the surface of the

p-type Co_3O_4, resulting in an enhancement in hole concentration and, consequently, a reduction in the overall resistance of the material. The sequential reactions can be represented as:

$$O_2(gas) \rightarrow O_2(adsorbed) \quad (3.4)$$

$$O_2(adsorbed) + e^- \leftrightarrow O_2^-(adsorbed) \quad (3.5)$$

$$CO\ (gas) \leftrightarrow CO\ (adsorbed) \quad (3.6)$$

$$O_2^-(adsorbed) + 2CO(adsorbed) \rightarrow 2CO_2(adsorbed) + e^- \quad (3.7)$$

Upon exposure to CO, a reducing gas, the interaction between the adsorbed CO molecules and surface O_2^- ions initiate a surface redox reaction. In this process, CO is oxidized to CO_2, accompanied by the release of trapped electrons back into the semiconductor. Since Co_3O_4 is a p-type material, the re-injection of electrons into the system reduces the hole concentration. This reduction in the majority carriers suppresses conductivity, ultimately causing an increase in the resistance of sensor. The CO-sensing performance is inseparably connected to the catalytic activity of Co^{3+} ions [58]. In the spinel structure of Co_3O_4, Co^{2+} ions occupy the tetrahedral coordination sites, whereas Co^{3+} ions are situated at the octahedral coordination sites [59].

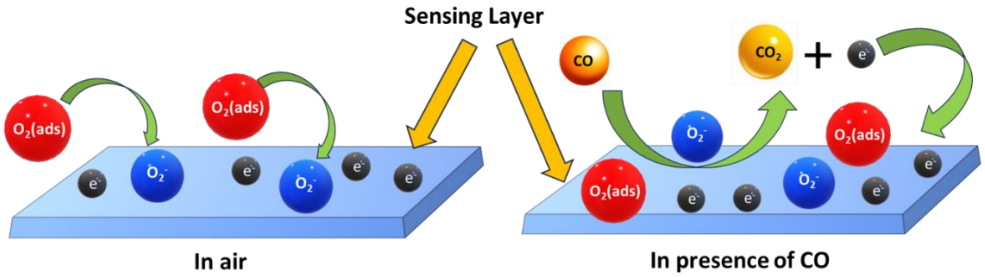


Fig. 3.11. Schematic diagram of sensing mechanism

While Co^{3+} ions occupy the octahedral coordination sites, numerous studies have demonstrated that they serve as the primary active centers for CO catalysis, whereas Co^{2+} ions are largely inactive. This behaviour is attributed

to the stronger oxidizing ability of Co^{3+} compared to Co^{2+} [60] Furthermore, the incorporation of Mo^{6+} ions into the Co_3O_4 lattice substitutes for Co sites, introduces excess electrons, and generates structural defects. The difference in oxidation states between Mo and Co promotes the creation of additional oxygen vacancies, thereby enhancing the number of active sites for oxygen adsorption. These synergistic effects of Mo^{6+}-induced oxygen vacancies, surface oxygen species, and the catalytic activity of Co^{3+} ions collectively dictate the improved CO-sensing performance of the material.

3.4. Conclusion

In this work, we have fabricated pristine-Co_3O_4, C-Co_3O_4 and C-Mo-Co_3O_4 via simple hydrothermal method for elevated sensing performance of CO gas at RT. The addition of CTAB and optimum amount of Mo doping shows a combined effect in enhancing the response in comparison to pristine Co_3O_4. The C-2.5% Mo-Co_3O_4 has depicted the best response of 4188% at 100 ppm CO at RT and sensitivity is 38.85% per ppm. The morphological transformation into nanoflowers and the two-fold increase in surface area relative to that for pristine-Co_3O_4 due to cationic surfactant CTAB and Mo doping has created more active sites for CO molecules to adsorb thereby enhancing the sensing response. The fabricated sensor demonstrates a LoD and LoQ values of 4 and 12 ppb, respectively. Moreover, the ease of fabrication of the sensor, its exceptional response, repeatability, reproducibility and long-term stability make it a suitable sensor for environmental monitoring of CO.

3.5. Reference

[1] S. Zhu et al. "Mechanism study on extraordinary room-temperature CO sensing capabilities of Pd-SnO_2 composite nanoceramics." Sensors and Actuators B: Chemical, vol. 285, pp. 49-55, 2019.

[2] B. Mandal et al. "Organo-di-benzoic-acidified ZnO nanohybrids for highly selective detection of CO at low temperature." The Journal of Physical Chemistry C, vol. 124, no. 13, pp. 7307-7316, 2020.

[3] R.M. Hall et al. "A summary of research and progress on carbon monoxide exposure control solutions on houseboats." Journal of occupational and environmental hygiene, vol. 11, no. 7, pp. D92-D100, 2014.

[4] N. Joshi et al. "A review on chemiresistive room temperature gas sensors based on metal oxide nanostructures, graphene and 2D transition metal dichalcogenides." Microchimica Acta, vol. 185, no. 4, pp. 213, 2018.

[5] Y. Wang et al. "A gas sensor based on Ag-modified ZnO flower-like microspheres: Temperature-modulated dual selectivity to CO and CH_4." Surfaces and interfaces, vol. 24, pp. 101110, 2021.

[6] A. Aaryashree et al. "Mesoporous tyrosine functionalized BTC-ZnO composite for highly selective capacitive CO sensor." IEEE Sensors Journal, vol. 21, no. 3, pp. 2610-2617, 2020.

[7] N. Luo et al. "Enhanced CO sensing properties of Pd modified ZnO porous nanosheets." Chinese Chemical Letters, vol. 31, no. 8, pp. 2033-2036. 2020.

[8] R.J. Rath et al. "Chemiresistive sensor for enhanced CO_2 gas monitoring." ACS sensors, vol. 9, no. 4, pp. 1735-1742. 2024.

[9] T. Baidya et al. "Ultra-low-temperature CO oxidation activity of octahedral site cobalt species in Co_3O_4 based catalysts: unravelling the origin of the unique catalytic property." The Journal of Physical Chemistry C, vol. 123, no. 32, pp. 19557-19571, 2019.

[10] T. Sen et al. "Room temperature CO sensing by polyaniline/Co_3O_4 nanocomposite." Journal of Applied Polymer Science, vol. 133, no. 42, 2016.

[11] D. Patil et al. "Highly sensitive and fast responding CO sensor based on Co3O4 nanorods." Talanta, vol. 81, no.1-2, pp. 37-43, 2010.

[12] C. Wang et al. "Metal oxide gas sensors: sensitivity and influencing factors." Sensors, vol. 10, no. 3, pp. 2088-2106, 2010.

[13] N. R. Khalid et al. "Electrochemical study of Mo-doped Co3O4 nanostructures synthesized by sol–gel method." Journal of Materials Science: Materials in Electronics, vol. 32, no. 3, pp. 3512-3521, 2021.

[14] P. M. Kouotou et al. "CVD-Made Spinels: Synthesis, Characterization and Applications for Clean Energy." Magnetic Spinels—Synthesis, Properties and Applications, 2017.

[15] S. Farhadi et al. "Synthesis, characterization, and investigation of optical and magnetic properties of cobalt oxide (Co_3O_4) nanoparticles." Journal of Nanostructure in Chemistry, vol. 3, no. 1, pp. 69, 2013.

[16] A. W. Alrowaily et al. "Hydrothermally synthesized neodymium-doped Co_3O_4 nanostructures as electrode for supercapacitor applications." Journal of Materials Science: Materials in Electronics, vol. 36, no. 4, pp. 246, 2025.

[17] C. Lohaus et al. "Investigations on RF-magnetron sputtered Co_3O_4 thin films regarding the solar energy conversion properties." Journal of Physics D: Applied Physics 49, no. 15, 2016.

[18] M. De Conti et al. "An overview into advantages and applications of conventional and unconventional hydro (solvo) thermal approaches for novel advanced materials design." Materials Today Sustainability, vol. 23, pp. 100458, 2023.

[19] C. Qin et al. "Metal-organic frameworks-derived Mn-doped Co3O4 porous nanosheets and enhanced CO sensing performance." Sensors and Actuators B: Chemical, vol. 351, pp. 130943, 2022.

[20] S. Tao. Et al. "Tailoring the energy level of Co_3O_4 by heteroatoms implantation for high-performance xylene detection." Sensors and Actuators B: Chemical, vol. 421, pp. 136493, 2024.

[21] Q. Zhou et al. "Highly sensitive carbon monoxide (CO) gas sensors based on Ni and Zn doped SnO_2 nanomaterials." Ceramics International, vol. 44, no. 4, pp. 4392-4399, 2018.

[22] D. Bekermann et al. "Co_3O_4/ZnO nanocomposites: from plasma synthesis to gas sensing applications." ACS applied materials & interfaces, vol. 4, no. 2, pp. 928-934, 2012.

[23] Y. Liu et al. "A highly sensitive and fast-responding SnO_2 sensor fabricated by combustion chemical vapor deposition." Chemistry of materials, vol. 17, no. 15, pp. 3997-4000, 2005.

[24] Y. Liu, Ying, and M. Liu. "Ordered ZnO nanorods synthesized by combustion chemical vapor deposition." Journal of Nanoscience and Nanotechnology, vol. 7, no. 12, pp. 4529-4533, 2007.

[25] S. L. Jadhav et al. "Mo-doped porous Co_3O_4 nanoflakes as an electrode with the enhanced capacitive contribution for asymmetric supercapacitor application." Journal of Energy Storage, vol. 82, pp. 110540, 2024.

[26] C. Patel et al. "Photoactivated Pd-loaded WO_3 for enhanced H2S sensing." IEEE Sensors Journal, vol. 23, no. 12, pp. 12552-12558, 2023.

[27] B. Zhang et al. "Room temperature NO_2 gas sensor based on porous Co_3O_4 slices/reduced graphene oxide hybrid." Sensors and Actuators B: Chemical, vol. 263, pp. 387-399, 2018.

[28] P. Murugesh et al. "Design of Ce incorporated tricobalt tetroxide Co_3O_4 sensor with boosted gas sensing performance toward nitrogen dioxide." Journal of Materials Science: Materials in Electronics, vol. 35, no. 15, pp. 1010, 2024.

[29] L. Du et al. "Metal-organic framework-derived hierarchical flower-like Mo-doped Co_3O_4 for enhanced triethylamine sensing properties." Journal of Alloys and Compounds, vol. 900, pp. 163470. 2022.

[30] W. Yang et al. "Chemiresistive detection of xylene vapor using MOF-derived porous Co3O4 microrods activated by Mo^{6+} cations." Sensors and Actuators B: Chemical, vol. 422, pp. 136658, 2025.

[31] C. Su et al. "Controllable synthesis of heterostructured CuO–NiO nanotubes and their synergistic effect for glycol gas sensing." Sensors and Actuators B: Chemical, vol. 304, pp. 127347, 2020.

[32] F. Liu et al. "Porous ZnO ultrathin nanosheets with high specific surface areas and abundant oxygen vacancies for acetylacetone gas sensing." ACS applied materials & interfaces, vol. 11, no. 27, pp. 24757-24763, 2019.

[33] A. N. Naveen, and S. Selladurai. "Tailoring structural, optical and magnetic properties of spinel type cobalt oxide (Co_3O_4) by manganese doping." Physica B: Condensed Matter, vol. 457, pp. 251-262, 2015.

[34] G. Hitkari et al. "Synthesis of chromium doped cobalt oxide (Cr: Co_3O_4) nanoparticles by co-precipitation method and enhanced photocatalytic properties in the visible region." J. Mater. Sci. Eng, vol. 7, no. 419, pp. 2169-2222, 2018.

[35] A. Lakehal et al. "Tuning of the physical properties by various transition metal doping in Co_3O_4: TM (TM= Ni, Mn, Cu) thin films: A comparative study." Chinese journal of physics, vol. 56, no. 5, pp. 1845-1852, 2018.

[36] S. S. T. Selvi et al. "Influence of CTAB surfactant on structural and optical properties of CuS and CdS nanoparticles by hydrothermal route." Journal of Experimental Nanoscience, vol. 13, no. 1, pp. 130-143, 2018.

[37] Z. Wei et al. "Surface modification of Co_3O_4 nanosheets through Cd-doping for enhanced CO sensing performance." Microchimica Acta, vol. 191, no. 5, pp. 234, 2024.

[38] C. Qin et al. "Metal-organic frameworks derived porous Co_3O_4 dodecahedeons with abundant active Co^{3+} for ppb-level CO gas sensing." Applied Surface Science, vol. 506, pp. 144900, 2020.

[39] J. Jansson, "Low-temperature CO oxidation over Co_3O_4/Al_2O_3." Journal of Catalysis, vol. 194, no. 1, pp. 55-60, 2000.

[40] R. Kumar et al. "Surfactant-assisted WS_2 nanostructures for enhanced NO_2 sensing performance." IEEE Sensors Journal, vol. 24, no. 5, pp. 5813-5820, 2024.

[41] C. N Wang et al. "Advances in doped ZnO nanostructures for gas sensor." The Chemical Record, vol. 20, no. 12, pp. 1553-1567, 2020.

[42] Shen, Chenyu, Hongjian Liang, Ziyue Zhao, Suyi Guo, Yuxiang Chen, Zhenquan Tan, Xue-Zhi Song, and Xiaofeng Wang. "Mo-Doped $LaFeO_3$ Gas Sensors with Enhanced Sensing Performance for Triethylamine Gas." Sensors, vol. 24, no. 15, pp. 4851, 2024.

[43] Y. Chen et al. "Mo-Doped Co3O4 Nanostructures for Enhanced N-Butanol Sensing Performance." Chemosensors, vol. 13, no. 2, pp. 61, 2025.

[44] J. Xu et al. "Uniform ZnO nanorods can be used to improve the response of ZnO gas sensor." Materials Science and Engineering: B, vol. 150, no. 1, pp. 55-60, 2008.

[45] D. Srinivasan et al. "Room temperature detection of isopropyl alcohol using CTAB-assisted silver-doped ZnO nanorods as chemiresistive gas sensor." Ceramics International, vol. 50, no. 20, pp. 39666-39677, 2024.

[46] R. K. Bedi et al. "Room-temperature ammonia sensor based on cationic surfactant-assisted nanocrystalline CuO." ACS applied materials & interfaces, vol. 2, no. 5, pp. 1361-1368, 2010.

[47] D. Meng et al. "CTAB-Assisted Hydrothermal synthesis of WO_3 hierarchical porous structures and investigation of their sensing properties." Journal of Nanomaterials, vol. 2015, no. 1, pp. 393205, 2015.

[48] D. Zhang et al. "Carbon monoxide gas sensing at room temperature using copper oxide-decorated graphene hybrid nanocomposite prepared by layer-by-layer self-assembly." Sensors and Actuators B: Chemical, vol. 247, pp. 875-882, 2017.

[49] R. Nadimicherla et al. "SnO_2 doped MoO_3 nanofibers and their carbon monoxide gas sensing performances." Solid State Ionics, vol. 300, pp. 128-134, 2017.

[50] D. Wang et al. "Gas sensing performance of carbon monoxide sensor based on rod-shaped tin diselenide/MOFs derived zinc oxide polyhedron at room temperature." Sensors and Actuators B: Chemical, vol. 371, pp. 132481, 2022.

[51] R. Xie et al. "Carbon monoxide gas sensing properties of SnO_2 modified metal-organic skeleton derived NiO." Sensors and Actuators A: Physical, vol. 367, pp. 115038, 2024.

[52] Z. Yang et al. "Carbon monoxide gas sensing properties of metal-organic frameworks-derived tin dioxide nanoparticles/molybdenum diselenide nanoflowers." Sensors and Actuators B: Chemical, vol. 304, pp. 127369, 2020.

[53] D. Zhang et al. "Construction and DFT study of Pd decorated WSe_2 nanosheets for highly sensitive CO detection at room temperature." Sensors and Actuators B: Chemical, vol. 360, pp. 131634, 2022.

[54] Y. Wu et al. "Selective detection of trace carbon monoxide at room temperature based on CuO nanosheets exposed to (111) crystal facets." Journal of Hazardous Materials, vol. 442, pp. 130041, 2023.

[55] D. N. Oosthuizen et al. "Selective detection of CO at room temperature with CuO nanoplatelets sensor for indoor air quality monitoring manifested by crystallinity." Applied Surface Science, vol. 466, pp. 545-553, 2019.

[56] A. K. Basu et al. "α-Fe_2O_3 loaded rGO nanosheets based fast response/recovery CO gas sensor at room temperature." Applied Surface Science, vol. 465, pp. 56-66, 2019.

[57] X. Peng, et al. "Boron-doped diamond nanowires for CO gas sensing application." Sensors and Actuators B: Chemical, vol. 241, pp. 383-389, 2017.

[58] Z. Wei, et al. "Surface modification of Co3O4 nanosheets through Cd-doping for enhanced CO sensing performance." Microchimica Acta, vol. 191, no. 5, pp. 234, 2024.

[59] T. Baidya et al. "Ultra-low-temperature CO oxidation activity of octahedral site cobalt species in Co3O4 based catalysts: unravelling the origin of the unique catalytic property." The Journal of Physical Chemistry C, vol. 123, no. 32, pp. 19557-19571, 2019.

[60] Y. Cai et al. "Ultrathin, polycrystalline, two-dimensional Co3O4 for low-temperature CO oxidation." ACS Catalysis, vol. 9, no. 3, pp. 2558-2567, 2019.

Chapter 4

Benchmarking Commercial Gas Sensors Against Lab-Developed Devices

4.1 Introduction

Commercial gas sensors are widely used in industrial safety, environmental monitoring, domestic appliances, and automotive applications owing to their reliability, cost-effectiveness and ease of integration into electronic systems. Among the various types of commercially available gas sensors, MOX sensors are particularly popular because of their simple structure, low cost, and capability to detect a wide range of gases. These sensors typically consist of a sensing material deposited on a ceramic substrate integrated with a heater, electrodes, and protective layers that facilitate stable operation. When exposed to target gases, the interaction between the gas molecules and the sensing material leads to a change in the electrical resistance of the sensor, which forms the basis of gas detection. One of the widely used commercial gas sensors for carbon monoxide detection is the MQ7 sensor. This sensor employs tin oxide (SnO_2) as the active sensing material and operates based on the resistance change of the sensing layer in presence of CO gas. The MQ7 sensor is commonly utilized in portable gas detectors, air quality monitoring devices, and safety systems due to its affordability and availability. However, commercial sensors often exhibit certain limitations such as moderate sensitivity, limited selectivity, and relatively high operating temperature requirements. In order to understand the working mechanism and performance characteristics of the commercial sensor, the MQ7 gas sensor was disassembled and its internal components were systematically examined. The structural components, including the sensing material, heater element, electrodes, and protective mesh, were carefully studied to gain insight into the sensor design and operation. Furthermore, the variation in electrical resistance of the sensing material upon exposure to CO gas was analyzed.

This chapter focuses on the performance of the commercial MQ7 sensor and comparison with the fabricated CTAB-assisted Mo-doped Co_3O_4 gas sensor.

A comparative analysis of the sensing characteristics, including sensitivity and selectivity, was carried out by monitoring the resistance change of both sensors under similar conditions. This comparison provides a deeper understanding of the advantages and performance improvements offered by the synthesized sensing material over conventional commercial gas sensors.

4.2. Structure and Working Principle of the MQ7 Commercial Gas Sensor

The MQ7 gas sensor belongs to the widely used MQ-series of MOX gas sensors designed for detecting different gases. These sensors are known for their simple design, durability, and ability to operate in a variety of environments. The MQ7 sensor is specifically developed for the detection of carbon monoxide (CO) and is commonly used in portable gas detectors and safety monitoring systems.

The sensing material used in the MQ7 sensor is tin oxide (SnO_2), which is an n-type semiconductor with high sensitivity to reducing gases. The sensing mechanism is based on the change in electrical resistance of the SnO_2 sensing layer when it interacts with gas molecules. In the presence of air, oxygen molecules adsorb on the surface of the sensing material and capture electrons from the conduction band, leading to an increase in resistance. When the sensor is exposed to carbon monoxide, the gas reacts with the adsorbed oxygen species, returning electrons to the conduction band and resulting a decrease in the resistance of the sensing layer [1].

Structurally, the MQ7 sensor consists of several key components that enable its sensing operation. The outermost part is a stainless-steel protective mesh, which acts as a protective barrier against dust and contaminants while allowing gas molecules to diffuse into the sensor. Beneath the mesh lies the sensing layer composed of SnO_2, which is deposited on a porous ceramic tube substrate that provides mechanical support and thermal insulation [2]. Inside the ceramic tube, a heating coil is embedded to maintain the sensing material at the required operating temperature for effective gas detection. The sensor

also contains electrode leads and external pins that provide electrical connections for measuring the resistance of the sensing material. The combined functioning of these components allows the MQ7 sensor to detect carbon monoxide through measurable resistance variations [2].

4.3. Disassembling, Electrical Characterization, and Comparative Analysis of the MQ7 Sensor

To understand the internal structure and sensing behaviour of the commercial MQ7 gas sensor, four MQ7 sensors were carefully dismantled and examined (Fig. 4.1). The outer stainless-steel protective mesh was first removed to expose the internal sensing assembly. Under backlight illumination, the internal structure revealed a ceramic tube coated with the sensing material along with an embedded heating element. The sensing material is most likely SnO_2, which is commonly used in MQ-series gas sensors due to its sensitivity toward reducing gases [3]. The heating element located inside the ceramic tube is responsible for maintaining the required operating temperature of the sensing layer and was observed to be made of Ni-Cr alloy [3]. The MQ7 sensor consists of six external pins, out of which four pins are connected to the sensing electrodes (sensor contact pads) and two pins are connected to the heater. The sensor contact pads are used to measure the resistance of the sensing layer, while the heater pins are used to apply voltage to the heating coil in order to maintain the operating temperature required for gas sensingIn this study, the resistance of the sensing material was measured by connecting a source meter to the sensor contact pads, allowing the change in resistance to be monitored during gas exposure, while the integrated heater was simultaneously powered using a 5 V DC supply throughout the experiment. To evaluate the sensing performance, selectivity studies were carried out using different gases including CO, NH_3, NO_2, SO_2, NO, and CO_2.

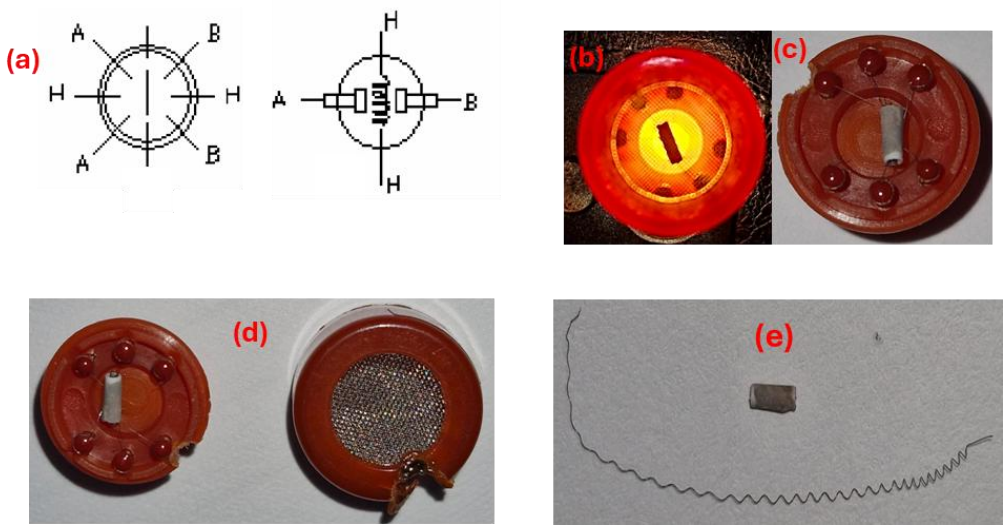


Fig. 4.1. (a) Image showing configuration of MQ7 sensor pins and structure of MQ7 sensor, (b) Image showing Internal structure of sensor under backlight illumination, (c) Internal structure of sensor (d) Internal and external structure of sensor in disassembled condition, (e) Heating coil and sensing material of the sensor

The sensing response was calculated using the formula $\frac{R_g - R_a}{R_a}$ x 100%, where R_g represents the resistance of the sensor in the presence of the target gas and R_a represents the baseline resistance in air. The experimental results showed that the responses of the MQ7 sensors varied significantly for different gases. A comparison was then performed between the commercial MQ7 sensors and the fabricated CTAB-assisted Mo-doped Co_3O_4 gas sensor developed in this work (Fig. 4.2). The fabricated sensor exhibited a response value of 4188% toward CO under similar experimental conditions, exhibiting a response approximately 32 times greater in comparison with the commercial MQ-7 gas sensor. While the commercial MQ7 sensors demonstrated measurable responses toward CO, the response values varied significantly across different sensors and were often higher for other gases such as NO_2, NO.

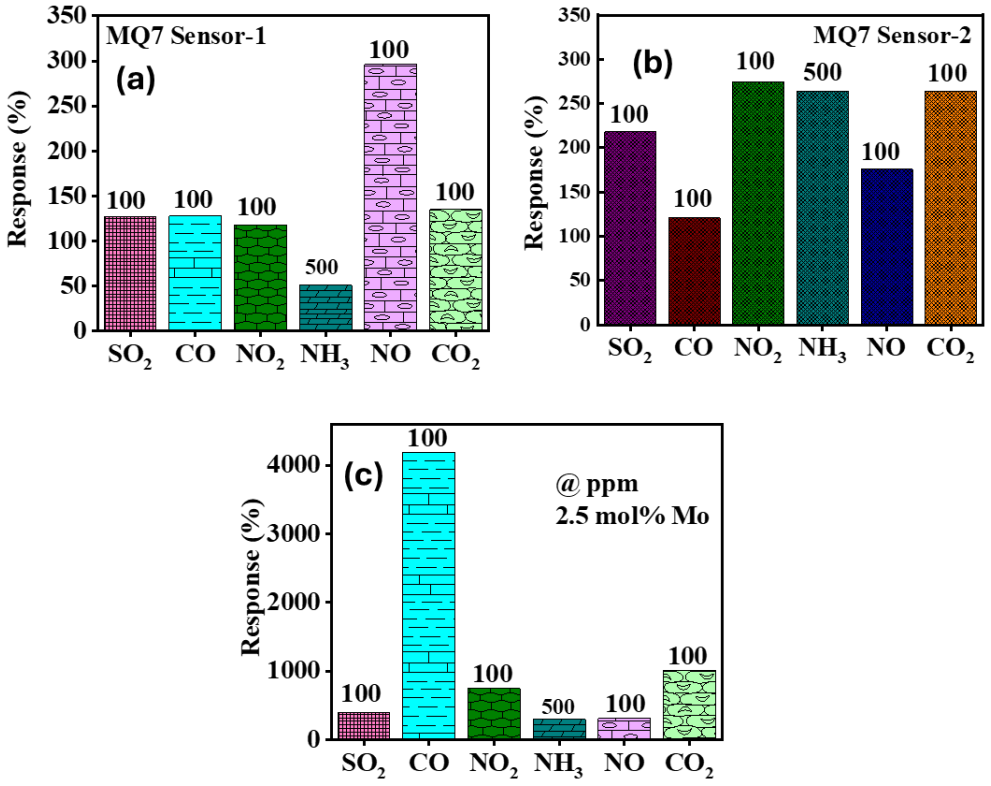


Fig. 4.2. Selectivity analysis of (a) 1st MQ7 sensor (b) 2nd MQ7 sensor (c) CTAB-assisted 2.5 mol% Mo-doped Co_3O_4

In contrast, the fabricated sensor demonstrated stable sensing characteristics with improved selectivity toward CO. Overall, the comparative analysis indicates that although commercial MQ7 sensors are widely used due to their affordability and ease of integration, they often exhibit cross-sensitivity toward multiple gases. The CTAB-assisted Mo-doped Co_3O_4 sensor developed in this work shows improved selectivity and reliable sensing performance toward CO, highlighting its potential for practical gas sensing applications.

4.4. Conclusion

In this chapter, a detailed study of the commercial MQ7 gas sensor was carried out to understand its structural design and sensing characteristics. The internal components of the sensor were examined by carefully dismantling the device, which revealed the presence of key elements such as the

protective mesh, SnO_2 sensing layer deposited on a ceramic tube, and the embedded Ni-Cr heating element responsible for maintaining the required operating temperature. The six-pin configuration of the sensor was also analyzed, where four pins were associated with the sensing electrodes and two pins were connected to the heater. The sensing response of the MQ7 sensor was evaluated by monitoring the change in resistance of the sensing layer upon exposure to different gases including CO, NH_3, NO_2, SO_2, NO, and CO_2. The obtained results indicated that the MQ7 sensor exhibits noticeable responses not only toward CO but also toward several other gases, suggesting the presence of cross-sensitivity. A comparative analysis was then performed between the commercial MQ7 sensor and the fabricated CTAB-assisted Mo-doped Co_3O_4 gas sensor developed in this work. The fabricated sensor demonstrated a response value of 4188% toward CO under similar testing conditions and exhibited improved selectivity compared to the commercial sensor. These observations indicate that while commercial MQ7 sensors are widely used due to their low cost and easy availability, their sensing performance can be limited by cross-sensitivity and inconsistent selectivity.

4.5. References

[1] R. Kumar et al. "SnO_2-based NO_2 gas sensor with outstanding sensing performance at room temperature." Micromachines, vol. 14, no. 4, pp. 728, 2023.

[2] Y. Z. Kam and N. Nayan. "Study on Carbon Monoxide Detector using Conventional and Plasma-Treated Gas Sensor." Evolution in Electrical and Electronic Engineering, vol. 2, no. 2, pp. 29-37, 2021.

[3] R. Rumantri et al. "Design and characterization of low-cost sensors for air quality monitoring system." Jurnal Pendidikan IPA Indonesia, vol. 7, no. 3, pp. 347-354, 2018.

Chapter 5
Conclusion and Future Scope

5.1 Conclusion

The principal achievement of this thesis lies in the development of highly sensitive metal oxide semiconductor-based gas sensing materials for the detection of CO. CTAB-assisted Mo-doped Co_3O_4 nanostructures synthesized via a hydrothermal method have been employed as the active sensing material. The study focuses on improving the sensing performance through Mo doping and surfactant-assisted nanostructure engineering. A comparative analysis with a commercial CO sensor (MQ7) has also been carried out to evaluate the sensitivity and selectivity of the fabricated sensor. The major outcomes of this thesis are outlined below:

Room-Temperature CO Detection Using Facile CTAB - Assisted Mo - Doped Co_3O_4 Nanoflowers

A highly sensitive CO gas sensor based on CTAB-assisted molybdenum (Mo)-doped Co_3O_4 nanostructures, synthesized via hydrothermal method was fabricated. The incorporation of the surfactant CTAB along with controlled Mo doping was utilized to improve the morphology and sensing properties of Co_3O_4. To optimize the sensing performance, different Mo concentrations of 1.5 mol%, 2.5 mol%, and 3.5 mol% were introduced into the Co_3O_4 structure. Comprehensive material characterization was carried out using XRD, FESEM, BET, UV-Vis spectroscopy, and XPS to investigate the structural, morphological, and surface properties of the synthesized materials. The CTAB-assisted synthesis resulted in the formation of well-defined nanostructures with increased surface area, providing a larger number of active sites for gas adsorption. Among the fabricated sensors, 2.5 mol% Mo-doped Co_3O_4 exhibited the best sensing performance toward CO at room temperature (25 °C). The optimized sensor exhibited an exceptionally high response of 4188% toward 100 ppm CO, along with rapid response and recovery times. The sensor also exhibited a limit of detection (LoD) of 4 ppb,

indicating its capability to detect extremely low concentrations of CO. Furthermore, the sensor exhibited excellent repeatability over 10 cycles, maintained long-term stability for 60 days, and demonstrated good selectivity toward CO in the presence of interfering gases. The influence of relative humidity on the sensing performance was also investigated within a humidity range of 35% to 97.5% RH. The results revealed that the sensor response gradually decreased with increasing humidity levels, arising from the competitive adsorption of water molecules on the sensor surface.

Benchmarking Commercial Gas Sensors Against Lab-Developed Devices

Furthermore, a comparative analysis with a commercial CO sensor (MQ7) was carried out. The MQ7 sensor was completely disassembled, and its internal components were studied in detail. Sensitivity and selectivity analyses demonstrated that the fabricated CTAB-assisted Mo-doped Co_3O_4 sensor exhibits superior sensing performance compared to the commercial MQ7 sensor. The CTAB-assisted Mo-doped Co_3O_4 sensor exhibits a response approximately 32 times higher than that of the commercial MQ-7 sensor. Moreover, it operates effectively at room temperature, whereas the MQ-7 sensor shows a response only when the heater is actively powered. The enhanced sensing characteristics are primarily due to the combined effect of Mo doping and CTAB-assisted morphology control, which improves surface reactivity, charge mobility, and gas adsorption capability. These findings highlight the strong potential of the developed sensor for high-performance CO detection and environmental monitoring applications.

5.2 Future Scope

The research work carried out in this thesis has provided significant insights into the use of CTAB-assisted Mo-doped Co_3O_4 nanomaterials for gas sensing applications. However, there remain several aspects that can be further explored in future studies, which are outlined below.

- Fabricate different doped and surface functionalized nanomaterial to detect other toxic gases.

- Integration of developed sensor into compact, low-power portable sensing systems for real-time environmental monitoring.
- Integration with wireless and IoT platforms for remote monitoring and smart environmental sensing applications.